Unexpectedly Large Contribution of Oxygen to Charge Compensation Triggered by Structural Disordering: Detailed Experimental and Theoretical Study on a LiNbO–NiO Binary System

AUTHOR(S):

Fukuma, Ryutaro; Harada, Maho; Zhao, Wenwen; Sawamura, Miho; Noda, Yusuke; Nakayama, Masanobu; Goto, Masato; ... Yamagishi, Hirona; Ohta, Toshiaki; Yabuuchi, Naoaki

CITATION:

Fukuma, Ryutaro ...[et al]. Unexpectedly Large Contribution of Oxygen to Charge Compensation Triggered by Structural Disordering: Detailed Experimental and Theoretical Study on a LiNbO–NiO Binary System. ACS Central Science 2022, 8(6): 775-794

ISSUE DATE:

2022-06-22

URL:

http://hdl.handle.net/2433/274532

ACS central science

http://pubs.acs.org/journal/acscii

Research Article

Unexpectedly Large Contribution of Oxygen to Charge Compensation Triggered by Structural Disordering: Detailed Experimental and Theoretical Study on a Li_3NbO_4–NiO Binary System

Ryutaro Fukuma,[◓] Maho Harada,[◓] Wenwen Zhao, Miho Sawamura, Yusuke Noda, Masanobu Nakayama, Masato Goto, Daisuke Kan, Yuichi Shimakawa, Masao Yonemura, Naohiro Ikeda, Ryuta Watanuki, Henrik L. Andersen, Anita M. D'Angelo, Neeraj Sharma, Jiwon Park, Hye Ryung Byon, Sayuri Fukuyama, Zhenji Han, Hitoshi Fukumitsu, Martin Schulz-Dobrick, Keisuke Yamanaka, Hirona Yamagishi, Toshiaki Ohta, and Naoaki Yabuuchi*

Cite This: *ACS Cent. Sci.* 2022, 8, 775–794

Read Online

ACCESS | Metrics & More | Article Recommendations | Supporting Information

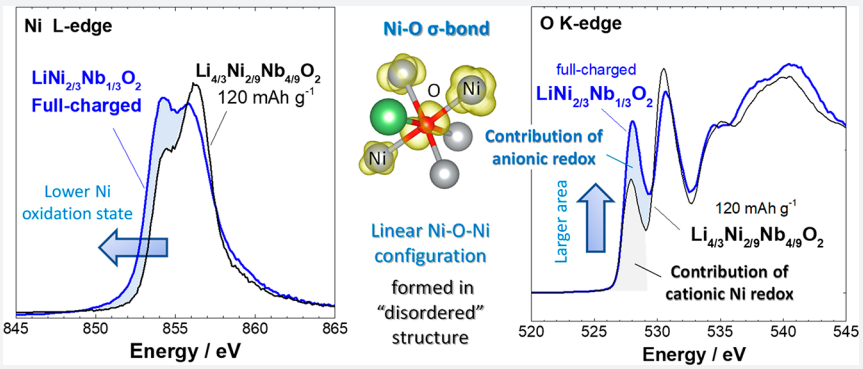

ABSTRACT: Dependence on lithium-ion batteries for automobile applications is rapidly increasing. The emerging use of anionic redox can boost the energy density of batteries, but the fundamental origin of anionic redox is still under debate. Moreover, to realize anionic redox, many reported electrode materials rely on manganese ions through π-type interactions with oxygen. Here, through a systematic experimental and theoretical study on a binary system of Li_3NbO_4–NiO, we demonstrate for the first time the unexpectedly large contribution of oxygen to charge compensation for electrochemical oxidation in Ni-based materials. In general, for Ni-based materials, *e.g.*, $LiNiO_2$, charge compensation is achieved mainly by Ni oxidation, with a lower contribution from oxygen. In contrast, for Li_3NbO_4–NiO, oxygen-based charge compensation is triggered by structural disordering and σ-type interactions with nickel ions, which are associated with a unique environment for oxygen, *i.e.*, a linear Ni–O–Ni configuration in the disordered system. Reversible anionic redox with a small hysteretic behavior was achieved for $LiNi_{2/3}Nb_{1/3}O_2$ with a cation-disordered Li/Ni arrangement. Further Li enrichment in the structure destabilizes anionic redox and leads to irreversible oxygen loss due to the disappearance of the linear Ni–O–Ni configuration and the formation of unstable Ni ions with high oxidation states. On the basis of these results, we discuss the possibility of using σ-type interactions for anionic redox to design advanced electrode materials for high-energy lithium-ion batteries.

■ INTRODUCTION

With three decades of history, lithium-ion battery (LIB) research and development is highly sophisticated,[1] with Ni-based layered materials[2−4] currently dominating the market for positive electrode materials. Currently, the lack of next-generation positive electrode materials, which practically outperform the Ni-based layered materials, hinders the further development of LIBs. Over the past decade, Li-excess manganese oxide, Li_2MnO_3, and its derivatives have been intensively studied as potential next-generation positive electrode materials for LIBs.[5−7] Anomalously large reversible

Received: March 2, 2022
Published: May 23, 2022

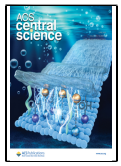

https://doi.org/10.1021/acscentsci.2c00238
ACS Cent. Sci. 2022, 8, 775–794

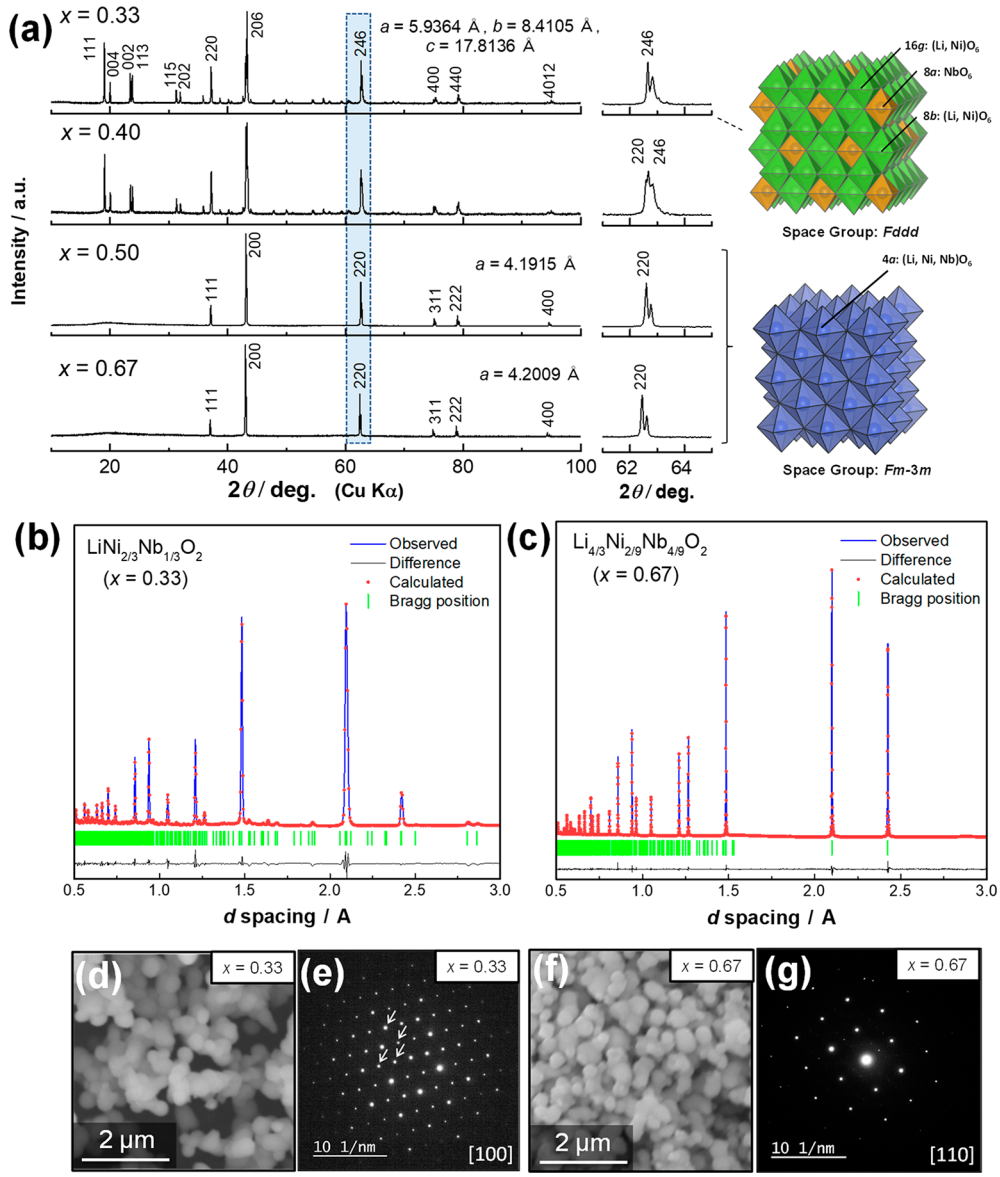

Figure 1. Structural and morphological characterization of the xLi$_3$NbO$_4$−(1 − x)NiO binary phase. (a) XRD patterns and schematic illustrations of the crystal structures. Enlarged patterns are also shown. Rietveld fits of structural models to neutron diffraction data for (b) LiNi$_{2/3}$Nb$_{1/3}$O$_2$ (x = 0.33) and (c) Li$_{4/3}$Ni$_{2/9}$Nb$_{4/9}$O$_2$ (x = 0.67). The samples used for the Rietveld analysis were synthesized at 1000 °C for 48 h. Peak splitting for the samples where x = 0.5 and 0.67 originates from a non-monochromatic X-ray source. SEM and ED patterns, respectively, of (d and e) LiNi$_{2/3}$Nb$_{1/3}$O$_2$ (x = 0.33) and (f and g) Li$_{4/3}$Ni$_{2/9}$Nb$_{4/9}$O$_2$ (x = 0.67). The samples used for The SEM and ED measurements were synthesized at 1000 °C for 2 h (also see Supporting Figure S6). Arrows in panel e correspond to superlattice reflections based on a parent rocksalt phase. Schematic illustrations of crystal structures were drawn using VESTA.[78]

capacities have been observed for these electrode materials[8−11] compared with classical and stoichiometric layered materials in which charge compensation during electrochemical Li extraction is achieved by reversible redox reactions of transition metal ions as cationic species. Significant research effort has revealed that charge compensation proceeds in both cationic and anionic species.[12,13] In a model system, Li$_2$Ru$_{1-x}$Sn$_x$O$_2$, the origin of the large reversible capacity (~260 mAhg^{-1}) was proposed to be the reversible formation of oxo- to peroxo-like species, namely anionic redox.[14] It has also been proposed that charge compensation is achieved by the formation of localized electron holes on oxygen atoms coordinated by Li$^+$ and Mn^{4+}.[15,16] A recent finding also suggests that the oxidation of oxygen results in the formation of oxygen molecules trapped in oxides, which are reduced back to oxide ions via reduction.[17] Nevertheless, for the Li$_2$MnO$_3$-based system, oxygen loss during the initial charge process and voltage decay during cycling are inevitable.[18] Oxygen loss activates Mn^{3+}/Mn^{4+} and Co^{2+}/Co^{3+} redox during electrochemical cycles, leading to a lower operating voltage.[19] The article morphology,[20] the surface coating,[21] the selection of a binder,[22] *etc.* influence voltage fading, but its suppression is a kinetically controlled phenomena. Relatively large voltage hysteresis for the charge−discharge process has also been noted.[23] Voltage hysteresis is influenced by in-plane cation ordering[17] and electron delocalization associated with the stabilization holes and the suppression of oxygen dimers.[24,25] Such disadvantages hinder the use of these high-capacity next-generation materials for practical applications. Other Li-excess systems, including Li$_4$MoO$_5$, Li$_3$NbO$_4$, and Li$_2$TiO$_3$, have been also proposed as host structures for anionic redox.[26−28]

https://doi.org/10.1021/acscentsci.2c00238
ACS Cent. Sci. 2022, 8, 775−794

Recently, the concept of anionic redox was extended to the Li-excess metal oxyfluorides with the rocksalt structure.[29−34] Oxygen loss during electrochemical cycles is partially mitigated by fluorination because of the increase in the contribution of Mn cationic redox.[35] Anionic redox has been evidenced not only for rocksalt-related structures but also for antifluorite-related structures[36−39] and metal silicates.[40]

Such oxygen redox chemistry potentially opens a new path to the design of energy storage materials, but many questions still remain unanswered. Theoretical studies of the Li-excess system have suggested that oxygen redox is activated in O 2p orbitals, which interact with excess Li ions in the transition metal layer (namely, oxygen redox occurs in compounds that contain linear Li^+-O-Li^+ environments).[16,41] Recently, this concept was extended to Mg^{2+}.[42] Ions with a highly ionic character donate more electrons to the oxygen O 2p orbital, thus the energy level of the O 2p orbital approaches the Fermi level. Therefore, oxygen redox is easily accessed at a lower electrochemical potential for compounds containing ions with a highly ionic bonding nature toward oxide ions, such as Mg^{2+}, Ti^{4+}, Nb^{5+}, *etc.*[43] Nevertheless, as pointed out in a recent article,[44] the nature of the chemical bonds between oxygen and the ions without valence electrons is essentially a nonbonding state, therefore these ions cannot stabilize the redox reaction of oxide ions. Oxygen redox chemistry was proposed to be energetically stabilized through π-type electron donation from Mn t_{2g} orbitals.[25,45] Therefore, the enrichment of ions with a d^0 configuration and an ionic bonding nature (*e.g.*, Nb^{5+} and Ti^{4+}) in the structure leads to the reduction in the number of oxide ions coordinated to transition metal ions (*e.g.*, Mn), which can stabilize anionic redox. To access oxygen redox at reasonable potentials (within the current electrolyte window), ions with d^0 configurations are critical; however, to ensure the reversibility of the redox process or stabilize the intermediate oxygen-based species, electron donation from metals such as Mn and Ni (those with d electrons) are critical. These two apparently opposing factors cause a dilemma regarding the design of materials with anionic redox for rechargeable battery applications. This provides opportunity for a careful materials design strategy that incorporates both d^0 and d^n transition metals in compounds.

In this work, detailed systematic studies are conducted on a binary system of Li_3NbO_4-NiO for lithium storage applications, taking full advantage of the anionic redox reaction. In our preliminary study on $Li_{1.3}Nb_{0.43}Ni_{0.27}O_2$, which is found in this binary system, its crystal structure and the electrochemical properties were reported.[46] Anomalously large voltage hysteresis during charge−discharge was noted and compared with $Li_{1.3}Nb_{0.3}Mn_{0.4}O_2$, suggesting that anionic redox is less stabilized for $Li_{1.3}Nb_{0.43}Ni_{0.27}O_2$. This work is a systematic study of this binary system, a Mn-free system. We report for the first time a significant the contribution of oxygen to the charge compensation mechanism. The formation of an oxygen unoccupied state was observed in stoichiometric $LiMeO_2$ (Me = Ni^{2+} and Nb^{5+}), and charge compensation by oxygen was unexpectedly large compared with that by nickel ions as cationic species. For conventional layered electrode materials with Ni ions, such as $LiNiO_2$ and $LiNi_{1/2}Mn_{1/2}O_2$, charge compensation is achieved mainly by Ni oxidation upon delithiation, and the contribution from oxygen is relatively small. The proposed process in the Ni or Nb system obviously differs from these conventional materials and is classified as anionic redox, where the oxidation reaction of oxygen is stabilized by a σ-type interaction with the Ni e_g orbital. Moreover, oxygen is reduced with a relatively small voltage hysteresis upon discharge (surprisingly less than 0.3 V, a value significantly smaller than that observed for the Mn system[47]). In contrast, for the Li-excess composition, $Li_{1.33}Me_{0.67}O_2$, oxygen loss is dominant as an irreversible process. These results indicate that anionic redox is energetically stabilized for the stoichiometric composition and Li enrichment in the structure results in destabilization. This trend is clearly different from the activation and stabilization processes of anionic redox in the Mn system that rely on the interaction between oxygen 2p and Mn t_{2g} orbitals, and this finding contributes to a better understanding of anionic redox with a different chemistry related to the oxygen coordination. From these results, we discuss the possibility of highly reversible anionic redox in the 4 V class of electrode materials.

RESULTS AND DISCUSSION

Structural and Morphological Characterization of the Li_3NbO_4-NiO Binary System. The crystal structures of the as-prepared samples were analyzed by both X-ray diffraction (XRD) and neutron diffraction (ND). Powder XRD patterns of the binary system of $xLi_3NbO_4-(1-x)NiO$ are shown in Figure 1. For the Li_3NbO_4-rich phases $Li_{4/3}Ni_{2/9}Nb_{4/9}O_2$ (x = 0.67) and $Li_{6/5}Ni_{2/5}Nb_{2/5}O_2$ (x = 0.50), diffraction lines were assigned as a cation-disordered rocksalt-type structure with a cubic symmetry ($Fm\bar{3}m$ space group). For the NiO-rich phase ($LiNi_{2/3}Nb_{1/3}O_2$, x = 0.33), major diffraction lines were also assigned as the rocksalt phase, but some additional diffraction lines were also observed in the 2θ range of 20−35°. All diffraction lines were successfully indexed to an orthorhombic lattice with a *Fddd* space group. These additional lines originate from Nb ordering at the octahedral sites of the rocksalt phase, and we note that the Nb ordering is within a common close-packed cubic lattice of oxide ions. The positions of the fundamental diffraction lines for the rocksalt phase gradually shift to higher diffraction angles as x decreases from 0.67 to 0.33, which is clearly visible in the highlighted 220 diffraction line in the 2θ range of 62−64°. Because the ionic radius of the Ni^{2+} ion (0.83 Å) is smaller than that of the Li^+ ions (0.90 Å) in an octahedral environment,[48] lattice parameters and the unit cell volume (in the rocksalt structure) gradually shrink as the NiO fraction increases. Detailed crystal structures of stoichiometric $LiNi_{2/3}Nb_{1/3}O_2$ and Li-excess $Li_{4/3}Ni_{2/9}Nb_{4/9}O_2$ were refined by the Rietveld analysis of structural models using both XRD and ND patterns. Results obtained from the ND data are shown in Figure 1b and c and the corresponding refined structural parameters are summarized in Supporting Tables S1 and S2, while the results derived from the XRD data are shown in Supporting Figure S1a and b and corresponding the structural parameters are also shown in Supporting Tables S1 and S2. The crystal structure of $LiNi_{2/3}Nb_{1/3}O_2$ is also consistent with the data reported in the literature.[49] Perfect Nb ordering is evidenced, while Ni and Li ions are essentially disordered in this structure. For $Li_{12/11}Ni_{6/11}Nb_{4/11}O_2$ (x = 0.40), broad diffraction lines suggest phase segregation, as shown in highlighted diffraction patterns of Figure 1a, and the sample consists of both *Fddd* and $Fm\bar{3}m$ phases. Mass fractions by calculated by Rietveld analysis to be 60% for the *Fddd* phase and 40% for the $Fm\bar{3}m$ phase. A single-phase sample was not obtained by applying the experimental conditions used in this study.

The particle morphology was further examined using SEM and TEM measurements. From SEM images of the stoichiometric and Li-excess samples, it was noted that the as-prepared

https://doi.org/10.1021/acscentsci.2c00238
ACS Cent. Sci. 2022, 8, 775−794

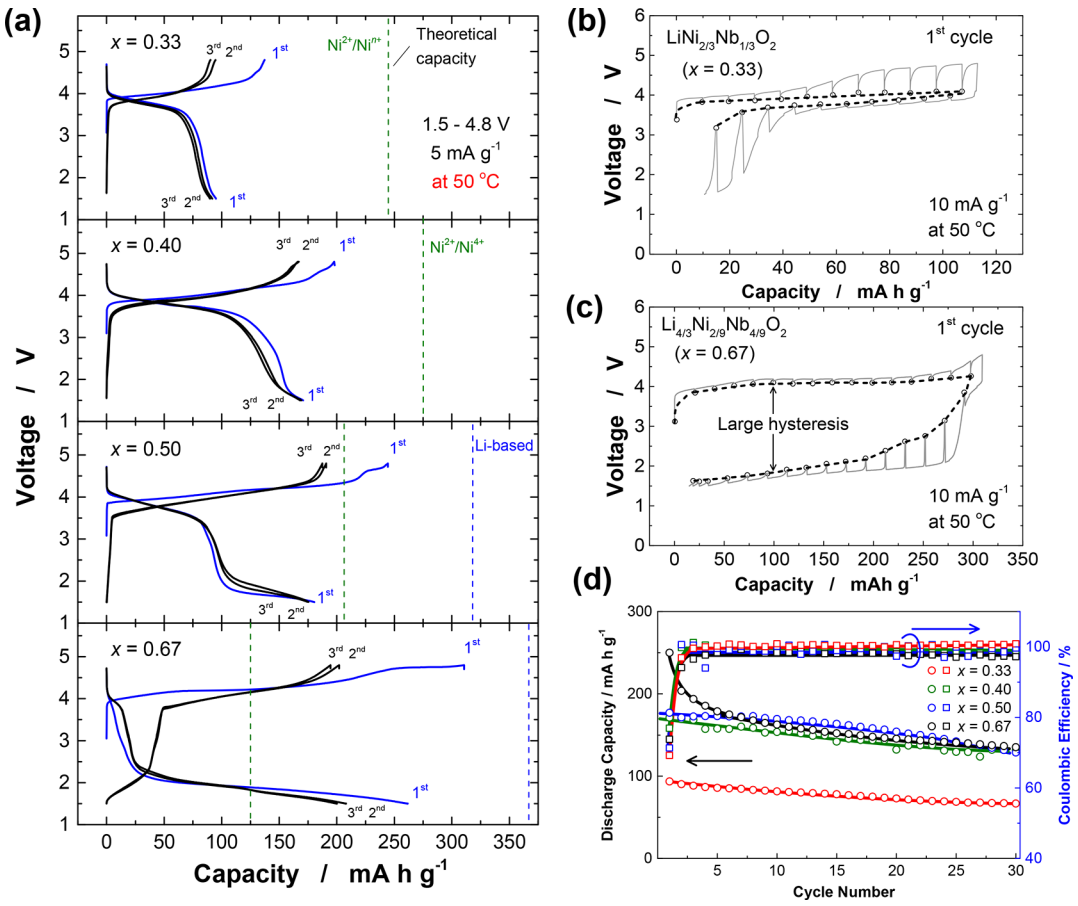

Figure 2. Electrochemical properties of $xLi_3NbO_4 - (1 - x)$ NiO binary phases in Li cells. The samples used herein were synthesized at 1000 °C for 2 h. (a) Charge−discharge profiles of Li−Ni−Nb−O samples cycled between 1.5 and 4.8 V at a specific current of 5 mA g^{-1}. Galvanostatic intermittent titration curves of (b) $LiNi_{2/3}Nb_{1/3}O_2$ ($x = 0.33$) and (c) $Li_{4/3}Ni_{2/9}Nb_{4/9}O_2$ ($x = 0.67$). The cells were charged for 1 and 2 h in $LiNi_{2/3}Nb_{1/3}O_2$ and $Li_{4/3}Ni_{2/9}Nb_{4/9}O_2$, respectively, then rested for 4 h. (d) Capacity retention and Coulombic efficiency of the binary system at a specific current of 5 mA g^{-1}.

samples had almost identical particle morphologies and particle sizes (~200 nm), as shown in Figure 1d and f. Spherical particles with a uniform size around 200 nm were observed for both samples. The difference in the chemical composition does not affect the particle morphology of the as-prepared samples in this system (also see Supporting Figure S2). Spherical particles with a smooth surface are also noted from TEM examinations, as shown in Supporting Figure S3. The particles are interconnected, which is clearly evidenced by the presence of grain boundaries. The selected area electron diffraction (SAED) patterns of stoichiometric $LiNi_{2/3}Nb_{1/3}O_2$ (Figure 1e) and Li-excess $Li_{4/3}Ni_{2/9}Nb_{4/9}O_2$ (Figure 1g) samples collected from the same zone axis on the base of a primitive rocksalt cell clearly indicatethea highly crystalline nature of both samples with well-defined diffraction spots. For the stoichiometric phase, both clear super-lattice reflections and fundamental rocksalt spots were observed, which is consistent with the results of Rietveld analysis associated with the Nb ordering. Further analysis, including the cation ordering of Nb ions in $LiNi_{2/3}Nb_{1/3}O_2$, of the SAED patterns is described in Supporting Figures S4 and S5. Note that a binary system of $Li_3NbO_4-(1 - x)CoO$ shows crystal structures and particle morphologies (under preparation) similar to those of the Ni system. This fact indicates that the enrichment of the Li_3NbO_4 fraction disturbs the cation ordering in the cubic-close-packed array of oxide ions, energetically stabilizing the disordered rocksalt structure.

Electrochemical Properties within the Li_3NbO_4−NiO Binary System. Electrode performance of the binary phase in Li cells was examined using galvanostatic charge−discharge at 50 °C, and the results are summarized in Figure 2. Although the samples synthesized for a longer time (48 h) have higher degrees of cation ordering, their larger particle sizes result in poor electrode performance. as shown in Supporting Figure S6. Therefore, the electrode performance was examined for the samples synthesized at 1000 °C for 2 h. For stoichiometric $LiNi_{2/3}Nb_{1/3}O_2$, approximately 100 mA h g^{-1} of reversible capacity was observed at a rate of 5 mA g^{-1} at 50 °C, with an average redox potential of ~4 V and small polarization and voltage hysteresis. The small voltage hysteresis is further evidenced by the measurement of the quasi-open-circuit voltage (Figure 2b). The redox reaction for the stoichiometric phase is highly reversible, and the operating voltage reaches nearly 4 V. Nevertheless, the observed reversible capacity is smaller than the theoretical capacity (245 mA h g^{-1}), which is further discussed in a later section. In addition, the observed reversible capacity decreased to 60 mA h g^{-1} at a rate of 20 mA g^{-1} (Supporting Figure S7a), indicating that the stoichiometric sample had inferior electrode kinetics. Further increasing the fraction of Li_3NbO_4 led to an increase in the reversible capacity. Li-excess $Li_{4/3}Ni_{2/9}Nb_{4/9}O_2$ delivers a large initial charge capacity, over 300 mA h g^{-1}, which significantly exceeds the theoretical expectation on the basis of Ni^{2+}/Ni^{4+} redox. This observation

https://doi.org/10.1021/acscentsci.2c00238
ACS Cent. Sci. 2022, 8, 775−794

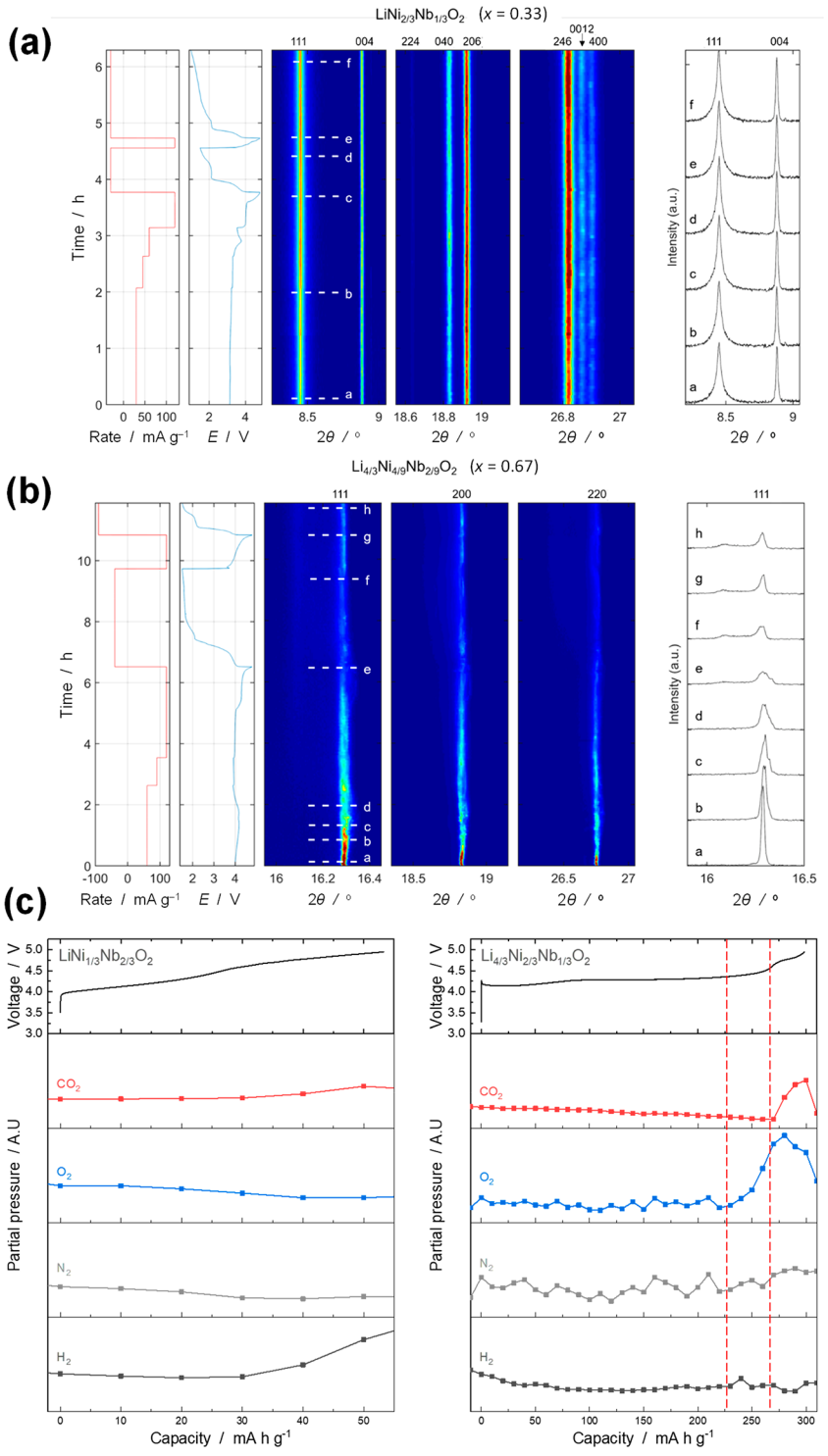

Figure 3. Selected regions of the *in operando* synchrotron XRD contour maps at 50 °C of the first two complete electrochemical cycles for (a) $LiNi_{2/3}Nb_{1/3}O_2$ ($x = 0.33$) and (b) $Li_{4/3}Ni_{2/9}Nb_{4/9}O_2$ ($x = 0.67$). The corresponding electrochemical load curves (current rate and voltage) are shown on the left. A new rocksalt phase with a low crystallinity appeared upon charge for the Li-excess sample. Also see the Supporting Information, including Supporting Figures S9 and S10, for more details. The same samples shown in Figure 2 were used for the analysis. (c) *In situ* partial gas pressures of CO_2, H_2, N_2, and O_2 from $LiNi_{2/3}Nb_{1/3}O_2$ and $Li_{4/3}Ni_{2/9}Nb_{4/9}O_2$ and the corresponding charge curves obtained at room temperature.

suggests that oxide ions are involved in the charge compensation process. Nevertheless, a large polarization with a capacity of 250 mA h g^{-1} was evidenced upon discharge. In addition, the poor reversibility of the electrode materials was observed, as shown in Figure 2d. To further examine the electrode reversibility of $Li_{4/3}Ni_{2/9}Nb_{4/9}O_2$, the initial charge capacities were changed from 100 to 300 mA h g^{-1}, followed by discharge to 1.5 V (Supporting Figure S7b). When the charge capacity was limited to 100 mA h g^{-1}, better reversibility was observed. As the charge capacity increased, the polarization upon discharge gradually increased, as can be seen from the appearance of a discharge plateau at 1.5−2.0 V. Notably, large hysteresis was still observed

https://doi.org/10.1021/acscentsci.2c00238
ACS Cent. Sci. 2022, 8, 775−794

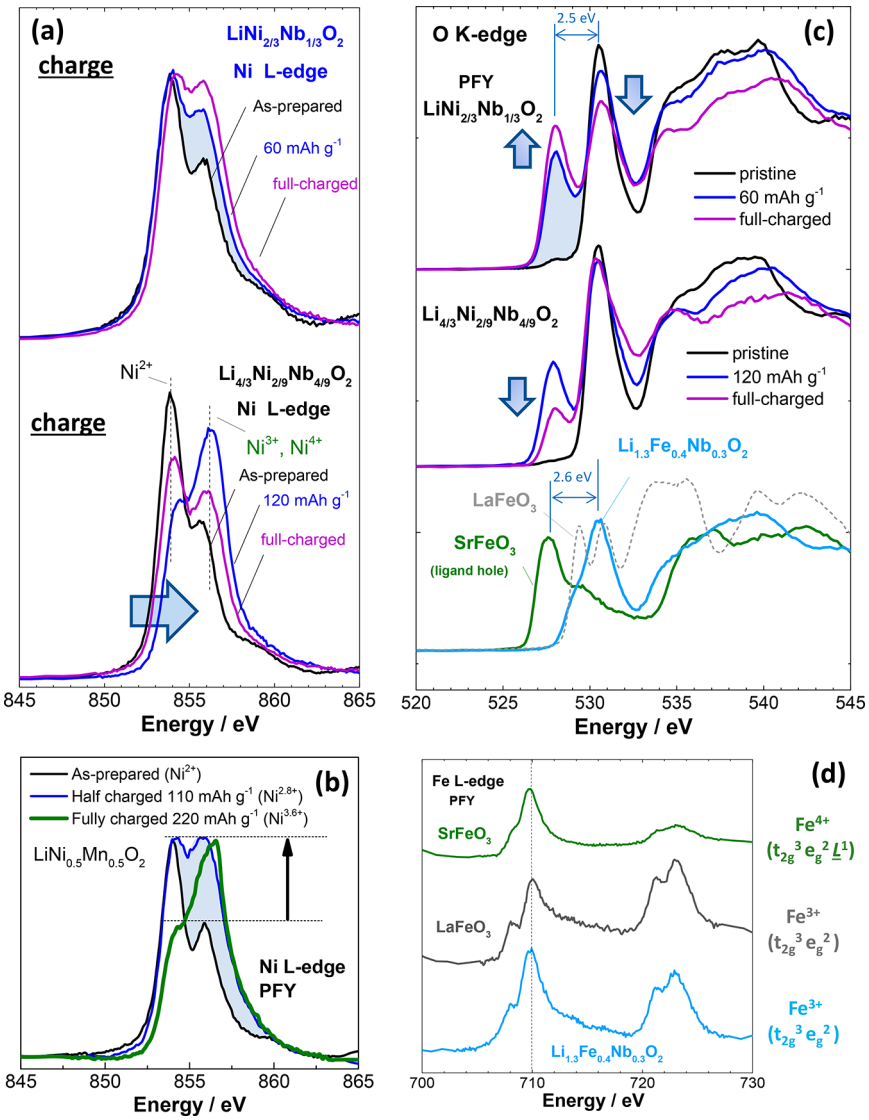

Figure 4. Variations of electronic structures of Ni and O in the electrochemical charge−discharge processes. (a) Change in the Ni L edge spectra of $Li_{1-y}Ni_{2/3}Nb_{1/3}O_2$ ($x = 0.33$) and $Li_{4/3-y}Ni_{2/9}Nb_{4/9}O_2$ ($x = 0.67$). (b) Change in the Ni L edge spectra of $Li_{1-y}Ni_{1/2}Mn_{1/2}O_2$. (c) Change in the O K edge XAS spectra of $Li_{1-y}Ni_{2/3}Nb_{1/3}O_2$ and $Li_{4/3-y}Ni_{2/9}Nb_{4/9}O_2$. As shown in blue shaded areas in panels a and c, for $Li_{1-y}Ni_{2/3}Nb_{1/3}O_2$, a more pronounced change was noted for the O K edge spectra compared with the Ni L edge spectra upon the initial charge to 60 mA h g^{-1}. O K edge XAS spectra of $SrFeO_3$ and $LaFeO_3$, which were used as reference materials for anionic redox, are also shown in panel c. The same samples shown in Figure 2 were used for the analysis. Changes in the O K edge XAS spectra for layered $LiNi_{1/2}Mn_{1/2}O_2$ as a reference material are shown in Supporting Figure S12, and the results for disordered $Li_{1-y}Ni_{2/3}Nb_{1/3}O_2$ and layered $Li_{1-y}Ni_{1/2}Mn_{1/2}O_2$ are compared in Supporting Figure S13. (d) Comparison of Fe L edge spectra of $SrFeO_3$, $LaFeO_3$, and $Li_{1.2}Fe_{0.4}Nb_{0.3}O_2$[55] with that of a disordered rocksalt structure.

in the open-circuit voltage measurements (Figure 2c), which will also be discussed in a later section.

Reaction Mechanisms of Samples in the Li_3NbO_4−NiO Binary System in Li Cells. To clarify differences found in the electrochemical properties, charge compensation and phase evolution processes of two structurally and compositionally distinct rocksalt phases, namely stoichiometric $LiNi_{2/3}Nb_{1/3}O_2$ ($x = 0.33$) and Li-excess $Li_{4/3}Ni_{2/9}Nb_{4/9}O_2$ ($x = 0.67$), were examined by *ex situ* and *in operando* XRD, OEMS, and *ex situ* XAS, as shown in Figures 1 and 2, respectively. The results of the *ex situ* XRD analysis are summarized in Supporting Section S1 and Supporting Figure S8. Highly reversible changes in the crystal structure of stoichiometric $Li_{1-y}Ni_{2/3}Nb_{1/3}O_2$ were noted from the XRD data during the charge−discharge process, whereas complicated phase evolution was observed for Li-excess $Li_{4/3-y}Ni_{2/9}Nb_{4/9}O_2$. These trends are further supported by the *in operando* synchrotron XRD experiments conducted for both oxides at 50 °C (see the Supporting Information). A contour map of $Li_{1-y}Ni_{2/3}Nb_{1/3}O_2$ ($x = 0.33$) obtained using *in operando* XRD is shown in Supporting Figure S9a, and enhancements of selected 2θ regions are plotted in Figure 3a. Similarly, a contour map and analyzed data of $Li_{4/3-y}Ni_{2/9}Nb_{4/9}O_2$ ($x = 0.67$) are also shown in Figure 3a and Supporting Figure S10. The samples exhibit quite different behaviors during electrochemical cycling. The *in operando* XRD study clearly reveals that $LiNi_{2/3}Nb_{1/3}O_2$ shows good structural stability, while the Li-rich $Li_{4/3}Ni_{2/9}Nb_{4/9}O_2$ undergoes irreversible structural degradation. The irreversible phase transition of $Li_{4/3-y}Ni_{2/9}Nb_{4/9}O_2$ is accompanied by the formation of a range of secondary isostructural phases, which are likely (partially) delithiated phases with different lattice parameters, crystallinities, and local strains. Closer inspection of the *in operando* XRD data (Figure

https://doi.org/10.1021/acscentsci.2c00238
ACS Cent. Sci. 2022, 8, 775−794

3a and Supporting Figure S10c and d) reveals that this involves a series of complex mechanisms or phase transitions, possibly including partial amorphization.

Gas generation related to phase evolution was measured by online electrochemical mass spectrometry (OEMS),[50] as shown in Figure 3c. Because excessive electrolyte vaporization at elevated temperatures resulted in the difficulty during the OEMS study, the measurement was conducted at room temperature. A smaller charge capacity with a larger polarization was observed for stoichiometric $LiNi_{2/3}Nb_{1/3}O_2$ ($x = 0.33$) at room temperature. An increase in the partial pressure of hydrogen, which originates from electrolyte decomposition, was observed at the higher voltage region (>4.5 V), but the evolution of O_2 and CO_2 gas was not detected. The diffusion of protic species generated by electrolyte oxidation from the positive electrode side to the metallic lithium negative electrode side and their subsequent reduction by metallic lithium result in hydrogen generation.[51] In contrast, oxygen generation was clearly observed for $Li_{4/3-y}Ni_{2/9}Nb_{4/9}O_2$ ($x = 0.67$) upon charge. An increase and decrease in the partial pressures of CO_2 and O_2, respectively, were observed at the higher voltage region, suggesting that oxygen released from the oxide upon charge further reacts with the electrolyte. Such irreversible reactions, including oxygen loss, are expected to be enhanced at elevated temperatures. Although the gas species generated in Li cells was qualitatively analyzed in this study, future work will target the use of a more quantitative approach[29] to OEMS.

Similar trends were also noted for the Ni K edge XAS data (Supporting Figure S11). For both compositions, the spectra of the as-prepared samples were found at an energy similar to that of divalent Ni ions. For $Li_{1-y}Ni_{2/3}Nb_{1/3}O_2$, the Ni K edge XAS spectra slightly shift to a higher energy region as charge capacity increases, indicating the partial oxidation of Ni^{2+}. Nevertheless, the shift of spectra is unexpectedly small when compared with that of a reference material of Ni^{3+} ($LiNiO_2$). This trend is also supported from the observation of Ni L edge spectra with the fluorescence yield mode (Figure 4a). Some extent of Ni oxidation was observed even after $Li_{1-y}Ni_{2/3}Nb_{1/3}O_2$ was charged to 4.8 V, but changes in the spectra are small compared with those of layered $Li_{1-y}Ni_{1/2}Mn_{1/2}O_2$ (Figure 4b). A much smaller change in the area of the XAS spectra was observed when compared with tat of the reference material, *i.e.*, half-charged $LiNi_{1/2}Mn_{1/2}O_2$ with $Ni^{2.8+}$. These observations suggest that the Ni ions remain at a lower average oxidation state (at least less than 3+) even after being charged to 4.8 V (also see Supporting Figures S12 and S13). This trend is further supported by the analysis of the extended X-ray absorption fine structure (EXAFS) spectra, as shown in Supporting Figure S14. The formation of Ni^{3+} ions, which are Jahn−Teller active,[52] is less evident for the stoichiometric sample even after charging. Moreover, after discharge to 1.5 V, the energy and profile of the spectrum are identical to that of the as-prepared sample. In addition, no change in the Nb K edge XAS spectra was noted during charging and discharging (Supporting Figure S15). The high reversibility of the XAS spectra at the Ni K edge is consistent with the XRD data and clearly shows that the contribution from Ni and Nb ions is unexpectedly small. As a result, the cationic redox reaction of Ni ions alone cannot explain the reversible redox reaction observed in Figure 2.

In contrast, complicated changes were observed for Li-excess $Li_{4/3-y}Ni_{2/9}Nb_{1/3}O_2$. When the sample was charged to ~120 mA h g^{-1}, the Ni K edge and L edge XAS spectra shifted to higher-energy regions, indicating the oxidation of the Ni ions. The average oxidation state is clearly higher than that of the Ni ions in the fully charged stoichiometric sample. When the sample was further charged to 4.8 V, the reduction of Ni ions was clearly evidenced in the Ni L edge XAS spectra. This is similar to the reduction of Ni upon "charge" that is associated with oxygen loss, which was reported in Li_2MnO_3-based positive electrodes.[53,54] Moreover, for the Li-excess system, the XAS spectrum at the Ni K edge shifts back to the lower energy region after discharge to 120 mA h g^{-1} and is found at nearly the same energy as the as-prepared sample. Upon further discharge, a drastic change is found in the spectrum, whose energy is lower than that of the as-prepared sample.When the spectrum of a Ni foil was compared for reference, it was thought that Ni^{2+} was partially reduced to a metallic state. From the Ni K edge spectra, it was expected that approximately 30% of Ni ions were reduced to the metallic state. This consideration is further supported by analysis of the EXAFS spectra (Supporting Figure S14). Similar to $Li_{4/3}Ni_{2/9}Nb_{1/3}O_2$, the reduction of Fe after discharge has been reported in the Fe system because of unavoidable oxygen loss upon charge.[54,55]

Nanostructures of the particles after electrochemical cycling were observed by TEM experiments. For stoichiometric $Li_{1-y}Ni_{2/3}Nb_{1/3}O_2$, no change was observed after electrochemical cycling, and high crystallinity was noted from its electron diffraction pattern (Supporting Figure S16a inset) after the sample was discharged to 1.5 V. In contrast, for Li-excess $Li_{4/3-y}Ni_{2/9}Nb_{1/3}O_2$, significant differences were observed before and after electrochemical cycling (Supporting Figure S16b). In the cores of the particles, a high crystallinity region with clear lattice fringes such as observed in the as-prepared sample was still found. However, the lattice fringes disappear at the edge of particles after discharge. A reduction of crystallinity at the edge and the formation of nanosized particles (less than 5 nm) were observed in the SAED pattern. These findings clearly indicate that a conversion reaction ($NiO + 2Li^+ + 2e^- \rightarrow Ni + Li_2O$) proceeds upon discharge, as expected from the XRD/XAS data, and also suggest that oxygen release occurs upon charge. The formation of metallic Ni is consistent with the results from the Ni K edge spectra after discharge. The reduction of Ni ions and the formation of Li_2O are also supported by the analysis of the Ni L edge and O K edge XAS spectra (Supporting Figure S17). Note that the reduction of Nb upon discharge is not evidenced by the XAS spectra (Supporting Figure S15). Following the charge, a new voltage plateau was observed at around 2 V (Figure 2a);a similar voltage profile was observed for nanosized NiO in Li cells with a conversion reaction.[56] Reoxidation of metallic or nanosized Ni results in the appearance of this new plateau at 2 V, coupled with larger polarization upon further charge, and thus poor reversibility as an electrode material, as shown in Figure 2d. Similar to this work, the formation of amorphous phases near the surfaces of the particles was reported in the Li_2MnO_3 system and found to be associated with irreversible oxygen loss during electrochemical cycling.[57]

Unexpectedly Large Contribution of Oxygen to Charge Compensation during Electrochemical Oxidation. For the stoichiometric phase, the contribution of Ni to charge compensation was unexpectedly limited. O K edge XAS spectra of these samples were, therefore, collected and analyzed. For stoichiometric layered materials containing Ni, for instance, $LiNiO_2$[58] and $LiCo_{1/3}Ni_{1/3}Mn_{1/3}O_2$,[59] some extent of peak shifting was observed in the O K edge XAS spectra after Li extraction, but minor changes were generally observed. O K

https://doi.org/10.1021/acscentsci.2c00238
ACS Cent. Sci. 2022, 8, 775−794

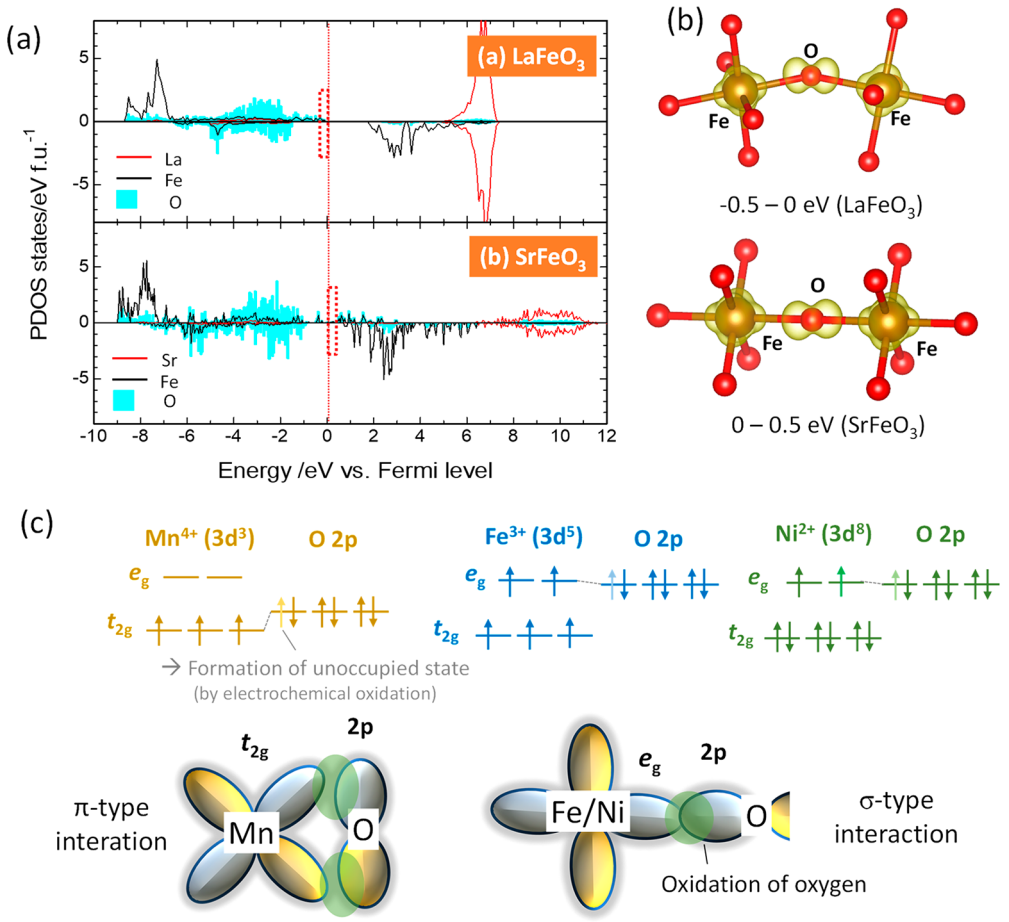

Figure 5. (a) Partial density of states (PDOS) of (a) $LaFeO_3$ and $SrFeO_3$. Positive and negative values for the PDOS indicate majority and minority spin states, respectively. (b) Visualized partial density of electronic states for the Fe−O−Fe arrangement in $LaFeO_3$ and $SrFeO_3$ near the Fermi level. The energy ranges from −0.5 to 0 vs the Fermi level and from 0 to 0.5 eV vs Fermi level for $LaFeO_3$ and $SrFeO_3$, respectively. The corresponding energy regions are indicated by red dotted lines in the panel a. (c) Based on the experimental observation of the O K edge spectrum of $SrFeO_3$ (Figure 4c), the pre edge peak at 527.5 eV corresponds to the formation of the unoccupied state of oxygen, which is stabilized through σ-type interactions with e_g electrons of Fe ions as visualized in panel b. Electron configurations of Mn^{4+}, Fe^{3+}, and Ni^{2+} in the O_h symmetry and schematic illustrations of π- and σ-type bonds are also shown.

edge XAS spectra of layered $Li_{1-y}Ni_{1/2}Mn_{1/2}O_2$ measured at the same beamline are also shown in Supporting Figure S12. The shift in energy is correlated with effective nuclear charges associated with the electrochemical oxidation of Ni, which hybridizes with the O 2p orbital to form σ-like bonds. In contrast to this observation, more pronounced changes in the profiles of the XAS spectra were observed in this binary system, as shown in Figure 4c. A new peak centered at 528 eV appears in the O K edge XAS spectra of stoichiometric $Li_{1-y}Ni_{2/3}Nb_{1/3}O_2$, and this peak grows as the charge capacity increases. A large difference in energy (2.5 eV) was observed for the new peak compared with the original peak centered at 530.5 eV. Note that this peak is clearly visible in the fluorescence yield mode, which is bulk-sensitive (see Supporting Figure S18). The change in the oxidation state of the Ni ions for the stoichiometric sample was small after the sample was charged to 60 mA h g^{-1}, as shown in Figure 4a, whereas a clear peak at 528 eV was observed in the O K edge XAS spectrum, as shown in Figure 4c. The appearance of this peak suggests that additional unoccupied states were formed in the O 2p orbital by electrochemical oxidation, *i.e.*, anionic redox and charge compensation by oxygen. It is noted that this peak at 528 eV was also observed for the Li-excess system after the sample was charged to 120 mA h g^{-1}, but the intensity of this peak decreased after the same was further charged to 4.8 V. This is consistent with the reduction of Ni ions upon charge (see Figure 4a and the K edge XAS spectra shown in Supporting Figure S11) and is most likely associated with oxygen loss for the Li-excess system, indicating that anionic redox is energetically destabilized for the Li-excess system. On the basis of these observations, it is proposed that a larger contribution to the charge compensation by anionic species was achieved, especially for the stoichiometric sample.

Experimental and Theoretical Analysis of Oxygen-Unoccupied States with Model Materials. In this study, $SrFeO_3$ with nominal Fe^{4+} prepared by the high-pressure method was selected as a model material with an unoccupied state of oxygen. The term "ligand hole" ($t_{2g}^3e_g^1 \approx t_{2g}^3e_g^2\underline{L}^1$) is also used to describe the unique electronic structure of oxygen in perovskite-type $SrFeO_3$.[60] In general, the oxygen0unoccupied state is not energetically stable, but the employed high-pressure approach allows us to synthesize $SrFeO_3$. For comparison, $LaFeO_3$ was also used as reference for Fe^{3+}, as it possesses the same perovskite structure as $SrFeO_3$. XRD patterns of as-prepared $SrFeO_3$ and $LaFeO_3$ are shown in Supporting Figure S19. The refined structural parameters are found in Supporting Table S3 and S4. The comparison of the XAS spectra of $SrFeO_3$

https://doi.org/10.1021/acscentsci.2c00238
ACS Cent. Sci. 2022, 8, 775−794

and $LaFeO_3$ clearly reveals that both perovskite oxides have quite similar profiles in the Fe L edge XAS spectr (Figure 4d), indicating that both Fe ions have an electronic structure similar to the high-spin d^5 state ($t_{2g}^3e_g^2$). In contrast, a significant difference was noted for the O K edge XAS spectra in Figure 4c. The energy of the pre-edge peak for $SrFeO_3$ is much lower (~2.6 eV) when compared with that of $LaFeO_3$. Moreover, the pre-edge peak observed for $SrFeO_3$ is close to the new peak found in $Li_{1-y}Ni_{2/3}Nb_{1/3}O_2$ after electrochemical oxidation. A similar trend in the O K edge spectra was also observed for $La_{1-x}Sr_xCrO_3$, where hole formation due to Sr substitution resulted in the transition from an insulator to a metal.[61]

To further study the electronic structures of $LaFeO_3$ and $SrFeO_3$, electron distributions of $LaFeO_3$ and $SrFeO_3$ were calculated using the Heyd−Scuseria−Ernzerhof (HSE06) hybrid functional calculation, and the results are summarized in Figure 5. Calculated Bader charges and net spin moments[62] of $LaFeO_3$ and $SrFeO_3$ are also summarized in Table 1. Similar

Table 1. Calculated Bader Charges and Net Spin Moments of $LaFeO_3$ and $SrFeO_3$[a]

	Bader charge		net spin moment (μ_B)	
atom	$LaFeO_3$	$SrFeO_3$	$LaFeO_3$	$SrFeO_3$
La or Sr	2.18	1.61	0.00	0.00
Fe	1.92	1.91	4.26	3.71
O	−1.37	−1.17	0.25	0.11

[a]La, Sr, and O (in $LaFeO_3$) ions are La^{3+}, Sr^{2+}, and O^{2-}, respectively, due to net-zero spin moments. Hole creation associated with the replacement of the La^{3+} ion ($LaFeO_3$) by the Sr^{2+} ion ($SrFeO_3$) occurs at both oxide ions and Fe ions due to change of Bader charges and net spin moments.

Bader charges were observed for the Fe ions of both oxides, while a lower negative charge for oxygen is observed in $SrFeO_3$. The net spin moment of Fe also decreased from 4.15 for $LaFeO_3$ to 3.71 for $SrFeO_3$. In addition, from the PDOS (Figure 5a) above the Fermi level (0−0.5 eV) and its calculated electron density (Figure 5b), relatively larger contributions of both Fe and O were noted for $SrFeO_3$. In the case of Mn^{4+}−O bonds in disordered rocksalt-type $Li_{1.3-x}Nb_{0.3}Mn_{0.4}O_2$, the PDOS just above the Fermi level mainly consists of O ions, with a minor contribution of manganese ions.[55] Such character originates from hole stabilization by a relatively weak π-type interaction between the Mn t_{2g} and O 2p orbitals (see Figure 5c).[44] In contrast, a strong σ-type interaction between Fe and O was observed for $SrFeO_3$, as shown in Figure 5b, indicating that the oxygen-unoccupied state is energetically stabilized by the formation of a chemical bond between the Fe e_g and O 2p orbitals. If a similar electron configuration occurs in the Ni system, the similar σ-type interaction with oxygen is anticipated.

Theoretical Understanding of Anionic Redox in $Li_{1-y}Ni_{2/3}Nb_{1/3}O_2$. *The Structural Model of $Li_{1-y}Ni_{2/3}Nb_{1/3}O_2$ Used for Computation.* The genetic algorithm (GA) approach[63] was used to explore energetically favorable cation arrangements for $LiNb_{1/3}Ni_{2/3}O_2$ and the delithiated phases $Li_{1-x}Nb_{1/3}Ni_{2/3}O_2$ (x = 0.17, 0.33, 0.50, 0.67, and 1.00). Details of the GA approach are described in Supporting Section S2. The superstructure model $Li_{18(1-x)}Nb_6Ni_{12}O_{36}$ with a rocksalt structure is considered in the present GA procedure. The lattice vectors a_{sc}, b_{sc}, and c_{sc} in the supercells correspond to linear combinations of lattice vectors a_p, b_p, and c_p in a primitive cell with a rocksalt structure, where $(a_{sc}\ b_{sc}\ c_{sc}) = (a_p\ b_p\ c_p)\ M_{sc}$. The supercell matrix M_{sc} was set as ash shown below to achieve agreement between experimental and computational compositions with reasonable computational costs.

$$M_{sc} = \begin{pmatrix} 3 & 0 & 0 \\ -1 & 3 & 0 \\ -1 & -1 & 4 \end{pmatrix}$$

It was also confirmed that the calculated Li removal voltage for this supercell was 0.08 V higher than that for the cell four-times larger than the original cell. Note that total energies of the models were evaluated during the GA procedure using DFT calculations with the GGA + U functional. As the calculation of total energies for the different models, around several thousand configurations, was needed, the DFT approach was the most economical. The U value for the Ni 3d states was set as 6.0 eV based on previous papers.[64,65] After GA cycles, the five lowest-energy configurations obtained from GA at each composition were recalculated using the HSE06 functional to estimate formation energies of delithiated systems.

Figure 6 shows (a) the energy distribution during the GA optimization and (b) the optimized structure of $LiNi_{2/3}Nb_{1/3}O_2$. Crystallographic information on $LiNi_{2/3}Nb_{1/3}O_2$, which was derived using the GA optimization, is also shown in Supporting Table S5. Figure 6c also shows distributions of the coordination number of nearest-neighboring (NN) Li−Li, Nb−Nb, and Ni−Ni bonds in $LiNi_{2/3}Nb_{1/3}O_2$, which were obtained using the GA-optimized structure (orange lines). Corresponding distribution profiles originating from the disordered structure, modeled using 36 000 cations sites, are presented (blue lines) for comparison. In the GA-derived structure, there is no NN Nb−Nb bond formation, whereas the disordered structure shows almost no isolated Nb ions. This fact indicates that Nb ions are structurally ordered in the GA-optimized structure. On the other hand, coordination number distributions for Li−Li and Ni−Ni interactions in the GA-derived structure are similar to those in the disordered structures. These structural features agree with the experimentally observed structure, where partial Nb ordering was observed for the sample prepared with a short heating time (Supporting Figure S6) while Ni and Li ions were essentially disordered, as mentioned previously. Thus, it was concluded that the GA-derived structure model was more appropriate in this study than a fully disordered structure.

Total energy changes of delihiated phases of $Li_{1-y}Nb_{1/3}Ni_{2/3}O_2$ were further computed. It is noted that only the Li/vacancy arrangement was considered in GA optimization of the delithiated phases because the migration of multivalent cations, namely Ni and Nb ions, is unlikely during electrochemical delithiation at 50 °C. The relaxed structures with the GA-optimized Li/vacancy arrangement shown no dimerization of oxygen atoms over the entire range of composition y ($0 \le y \le 1$ in $Li_{1-y}Nb_{1/3}Ni_{2/3}O_2$), as the minimum bond distance between two oxygen atoms is 2.53 Å (Supporting Figure S20). The phase stability of partially delithiated samples was evaluated by plotting the formation energies, ΔE_f, using energies of fully lithiated and delithiated compositions as references.[76,66]

$$\Delta E_f(y) = E_0(y) - (1-y)E_0(0) - yE_0 \quad (1)$$

where $E_0(y)$ corresponds to total energy of the compound with composition y evaluated using first-principles calculations with the HSE06 functional. Formation energies of the corresponding structures obtained using eq 1 are plotted in Figure 6d. Circle

https://doi.org/10.1021/acscentsci.2c00238
ACS Cent. Sci. 2022, 8, 775−794

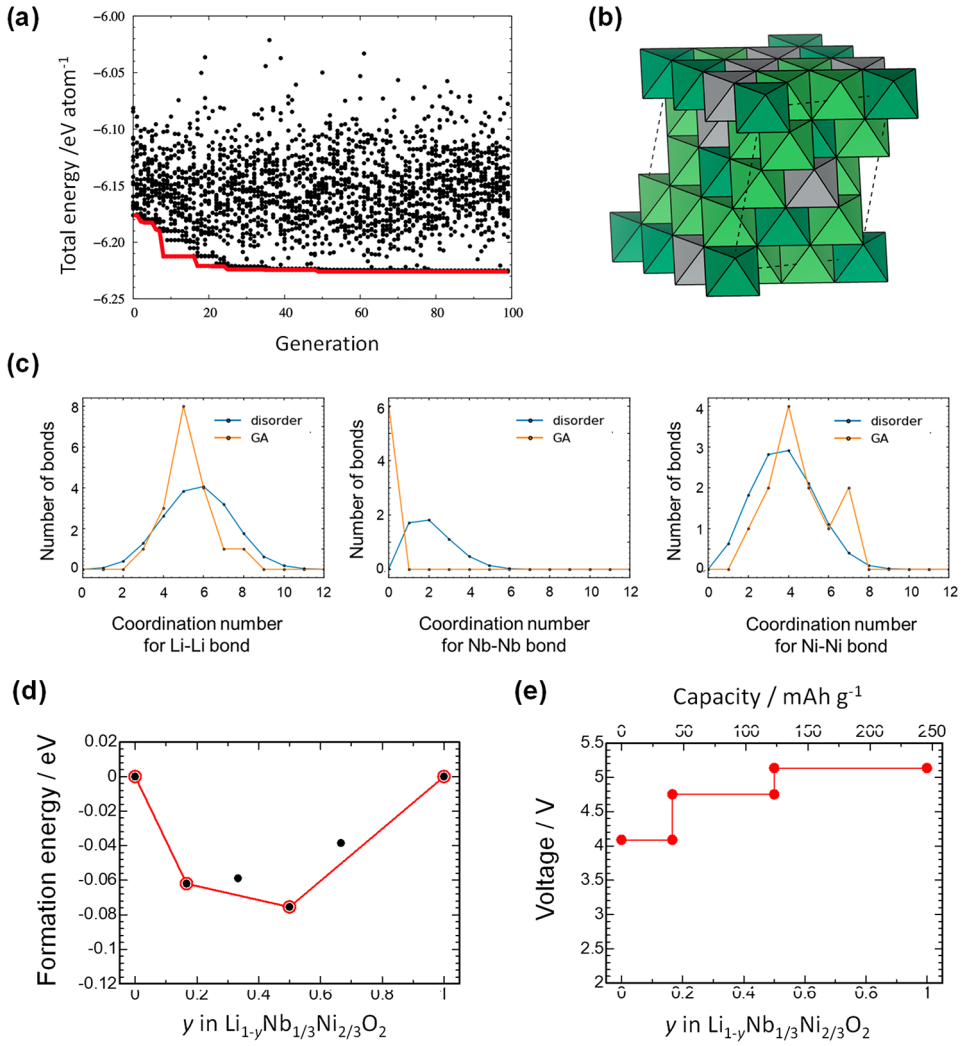

Figure 6. Structural optimization of $LiNi_{2/3}Nb_{1/3}O_2$ for theoretical calculations. (a) Total energy variations of $Li_{18(1-y)}Ni_{12}Nb_6O_{36}$ as a function of generation in the genetic algorithm (GA) procedure (also see Supporting Section S2 for the GA procedure). The red line indicates the lowest energy in each generation. (b) A schematic illustration of the crystal structure of $Li_{18}Ni_{12}Nb_6O_{36}$ obtained from GA, with partial cation ordering for Nb and disordered Li/Ni arrangements. Light green, dark green, and gray colored octahedra denote LiO_6, NbO_6, and NiO_6, respectively. Dotted lines correspond to a unit cell of $Li_{18}Ni_{12}Nb_6O_{36}$. (c) Distributions of the coordination number for NN Li−Li, Nb−Nb, and Ni−Ni bonds for $LiNi_{2/3}Nb_{1/3}O_2$, which were derived from GA optimization and cation-disordered models. (d) Formation energies of $Li_{1-y}Nb_{1/3}Ni_{2/3}O_2$ estimated from first-principles calculations with the HSE06 hybrid functional. The formation energies are normalized by each formula unit. (e) Calculated voltage profiles of $Li_{1-y}Ni_{2/3}Nb_{1/3}O_2$.

symbols indicate structures that are the most energetically stable at composition y. Tie lines in the figure represent the convex hull among the GA-optimized structures. The figure shows that several intermittent compositions of the calculated $Li_{1-y}Nb_{1/3}Ni_{2/3}O_2$ structures are thermodynamically stable, indicating that solid solution phases are formed upon delithiation; this is also consistent with the experimental finding. Delithiation voltages were also estimated according to the following methodology used in the literature:[67]

$$V(y) = [E_0(y) - E_0(y + z) - zE_0(\mathrm{Li})]/zF \quad (2)$$

where F stands for the Faraday constant and $E_0(y + z)$ and $E_0(\mathrm{Li})$ correspond to total energies of the compound with composition $y + z$ and the Li metal, respectively. It is noted that the voltages resulting from the computation (Figure 6e) range from ~4 to ~5 V, also showing agreement with the experimental results.

Analysis of Charge Compensation Mechanisms from Changes in the Partial Density of States. The partial density of states (PDOS) of each orbital and the partial electronic state densities for occupied and unoccupied states at several PDOS peaks for $Li_{1-y}Ni_{2/3}Nb_{1/3}O_2$ are shown in Figure 7a. For the stoichiometric phase $y = 0$, the PDOS near the Fermi level consists of both of O 2p and Ni e_g hybridized orbitals (arrow A in Figure 7a). Moreover, a linear Ni−O−Ni configuration with an antibonding character was found. This unique configuration was realized only for the disordered structure and was not formed for the layered structure. After Li extraction, $y = 0.33$, the PDOS of Ni 3d hybridized with O 2p orbitals appears at the bottom of the unoccupied states (arrow B in Figure 7a). Corresponding partial electron and hole densities clearly indicate the σ-type hybridization of the Ni 3d and O 2p orbitals. Even at the initial stage of charge, an obvious change was observed in the O 2p PDOS, which is consistent with the experimental observation. A contribution to the Ni 3d orbital from both sides of the O 2p

https://doi.org/10.1021/acscentsci.2c00238
ACS Cent. Sci. 2022, 8, 775−794

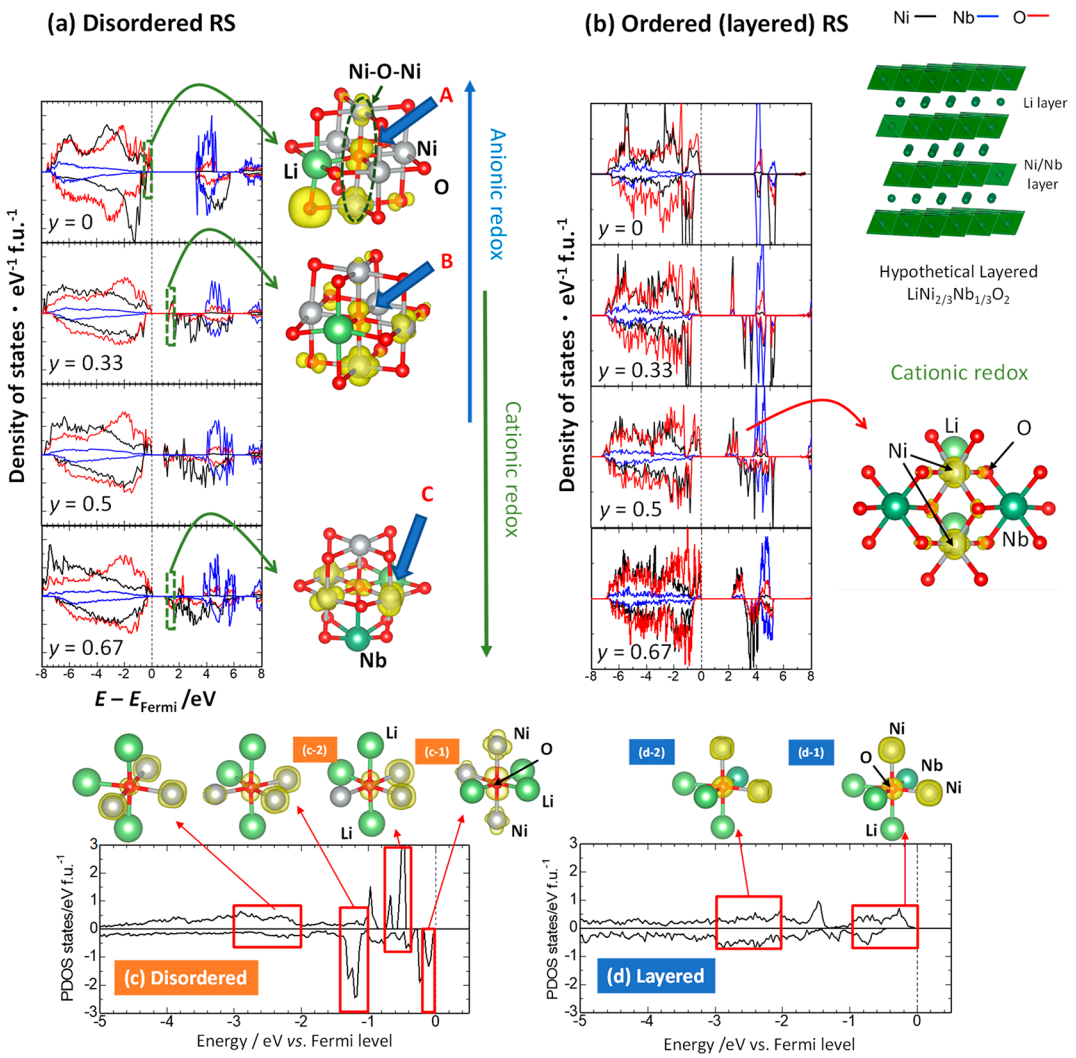

Figure 7. Electronic structure study of $LiNi_{2/3}Nb_{1/3}O_2$ with the cation disordered structure using DFT calculations. (a) PDOS results of disordered $Li_{1-y}Ni_{2/3}Nb_{1/3}O_2$ at different states of charge. Black, blue, and red lines indicate the PDOS for Ni, Nb and O ions, respectively. The visualized partial density of states for different compositions is also shown. (b) Data for hypothetical layered $Li_{1-y}Ni_{2/3}Nb_{1/3}O_2$. PDOSs for specific oxide ions in (c) disordered and (d) hypothetical layered $LiNi_{2/3}Nb_{1/3}O_2$ along with visualized electronic configurations. See the text for more details.

orbital was noted, but the pronounced presence of the O 2p orbital was also observed, indicating the formation of an unoccupied state for oxygen with the partial oxidation of Ni ions. This electronic configuration is expected to be analogous to that in $SrFeO_3$ (Figure 5) and is a σ-type interaction between Ni and O. Note that a linear Fe−O−Fe configuration is also formed in perovskite-type $SrFeO_3$. Further delithiation resulted in a different oxygen contribution trend, and an increase in the relatively large contribution from Ni ions was found in the PDOS for y = 0.67 (arrow C in Figure 7a). Cationic redox is more pronounced in the later delithiation process, which is further discussed in the next section.

To further emphasize the uniqueness of the linear Ni−O−Ni configuration formed in the disordered structure, electronic structures of a hypothetical material, "layered" $LiNi_{2/3}Nb_{1/3}O_2$, were computed, and the PDOSs of the layered and disordered samples are compared in Figure 7b (also see Supporting Section S3 and Supporting Figure S21). Figure 7b shows variations of the PDOSs of Ni, Nb, and O ions with respect to the composition y. The top of the valence bands mainly consists of Ni 3d and O 2p orbitals for the entire compositional range, indicating the hybridization of the Ni−O bonds. For comparison purposes, PDOSs of a specific oxide ion near the Fermi level were also computed for both disordered and ordered (layered) $LiNi_{2/3}Nb_{1/3}O_2$, and the electron densities are visualized in Figure 7c and d, respectively. For layered $LiNi_{2/3}Nb_{1/3}O_2$, the linear Ni−O−Ni configuration was not formed, and a clear bonding formation between Ni and O was not found (marked as "d-1" in Figure 7d). In contrast, for disordered $LiNi_{2/3}Nb_{1/3}O_2$, the PDOS near the Fermi level (−0.5−0 eV) mainly consists of ions with the linear Ni−O−Ni configuration and a σ-type bond (marked as "c-1" in Figure 7c); thus, the contribution of oxygen is more pronounced compared with that in layered $LiNi_{2/3}Nb_{1/3}O_2$. Moreover, a nonlinear Ni−O−Ni configuration (marked as "c-1") and a linear Li−O−Li configuration (marked as "c-2") were also found in disordered $LiNi_{2/3}Nb_{1/3}O_2$, but the energy relative to the Fermi level was lower for the linear Ni−O−Ni configuration. The linear Li−O−Li configuration with a nonbonding character is energetically stable compared with the linear Ni−O−Ni configuration with an antibonding character. After the delithiation of the layered phase, components consisting of Ni and O orbitals are visible at the bottom of the conduction bands. This was also confirmed by the visualized images of DOS in Figure 7b, where the top of the

https://doi.org/10.1021/acscentsci.2c00238
ACS Cent. Sci. 2022, 8, 775−794

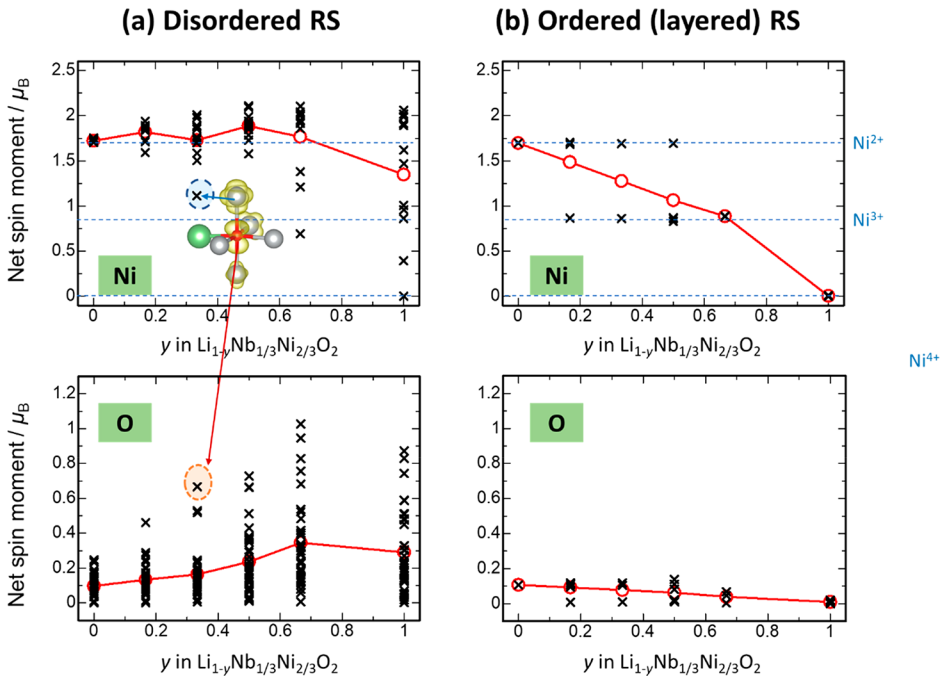

Figure 8. Estimated changes in the oxidation states of Ni and O ions during Li extraction from net spin moments. The data for (a) disordered $LiNi_{2/3}Nb_{1/3}O_2$ and (b) hypothetical layered $LiNi_{2/3}Nb_{1/3}O_2$ are shown. The net spin moments are defined as the difference between the up and down electron spins as a function of the integration radius (1.2 Å in this study) of the corresponding ion cores. Changes in the net spin moments for $LiNiO_2$ and NiO_2 are also shown in Supporting Figure S23. Red lines in the figure correspond on average to changes in the net spin moments.

valence band is at $y = 0.5$ and the bottom of the conduction band (unoccupied states) is at $y = 0.67$. In both images, larger contributions from Ni 3d orbitals are visible, and the contributions from the surrounding oxide ions are reduced when compared with those in the disordered phase in the early stage of charge.

Similar to $SrFeO_3$, net spin moments for Ni and O ions upon delithiation were computed to further estimate charge compensation mechanisms, and the results for the disordered and hypothetical layered samples are summarized in Figure 8. Figure 8a shows changes in the net spin moments of the Ni and O ions in disordered RS-type $Li_{1-y}Ni_{2/3}Nb_{1/3}O_2$ ($y = 0$, 0.17, 0.33, and 0.50). The majority of the net spin moments of Ni ions at composition $y = 0$ are distributed around >1.5, corresponding to the formal oxidation state of Ni, *i.e.*, 2+ ($t_{2g}^6 e_g^2$), and the net spin moments of several Ni ions decrease to ∼1.2 after the delithiation. Note that the net spin moments of some of Ni ions are reduced to *ca.* 1.2 for $y = 0.17$−0.33. These Ni ions originate from the partial oxidation of Ni ions in the linear Ni−O−Ni configuration. Nevertheless, the net spin moments of Ni ions are on average higher than those found for Ni^{3+} in the layered structure, as shown below. Moreover, the Ni oxidation states for $y = 0.33$ are on average (shown as a red line in the figure) close to those for $y = 0$. Relatively larger changes in Ni oxidation states from the spin moments are expected for $y > 0.33$, owing to the oxidation of Ni ions in nonlinear configurations. Complicated changes in the net spin moments indicate that many different local configurations of Ni ions are formed in the disordered structure, as shown in Figure 7c.

On the other hand, net spin moments of O ions are distributed around zero for stoichiometric and disordered RS-type $LiNi_{2/3}Nb_{1/3}O_2$, corresponding to a closed-shell electronic configuration, *i.e.*, oxide ions, O^{2-}. The electrochemical Li extraction causes a gradual increase in the net spin moments of the O ions, as shown in Figure 8, indicating both the oxidation of the O^{2-} ions and the lack of oxygen dimerization[68] for relaxed structures, as mentioned before. Note that oxide ions with relatively larger spin moments are found in oxygen with a linear Ni−O−Ni configuration (see the red hatched circle in Figure 8a). Moreover, the changes in the net spin moments for oxygen are unique for $Li_{1-y}Ni_{2/3}Nb_{1/3}O_2$ with the cation-disordered structure, and a similar observation was noted for $SrFeO_3$ with the linear Fe−O−Fe configuration (Figure 5b).

In contrast to the disordered structure, hypothetical layered $Li_{1-y}Ni_{2/3}Nb_{1/3}O_2$ has net spin moments for Ni ions that are discretely distributed and reduced from 1.6 to 0.8 at the compositional range of $0 \leq y \leq 0.67$, which corresponds to oxidation of Ni^{2+} ($t_{2g}^6 e_g^2$) to Ni^{3+} ($t_{2g}^6 e_g^1$) because net spin moments for N^{i2+} and Ni^{3+} are expected to be 2 and 1, respectively. Further delithiation at $y > 0.67$ causes the oxidation of Ni^{3+} to Ni^{4+} while the net spin moments for oxide ions are almost zero for the entire compositional range. Some of the oxide ions have nonzero spin moments (<0.1), owing to the strong hybridization between Ni and O ions. The calculated high-voltage profile (>5 V) at $y > 0.67$ in Supporting Figure S21b is ascribed to $Ni^{3+/4+}$ oxidation, and the contribution of O^{2-} oxidation is excluded on the basis of the net spin moments, which are clearly different from those of the cation-disordered rocksalt sample with the linear Ni−O−Ni configuration. Moreover, the average net spin moments of Ni ions are much higher for the the disordered structure, indicating the Ni oxidation states are lower. Supporting Figure S22 shows variations of Barder charges for Ni and O ions in (a) disordered and (b) ordered (layered) RS-type $Li_{1-y}Ni_{2/3}Nb_{1/3}O_2$. The trend of Bader charges supports the above results of the net spin moment shown in Figure 8. For example, the oxidation of several oxide ions is clearly visible in disordered $Li_{1-y}Ni_{2/3}Nb_{1/3}O_2$, while no significant variation of Bader charges for oxide ions is

https://doi.org/10.1021/acscentsci.2c00238
ACS Cent. Sci. 2022, 8, 775−794

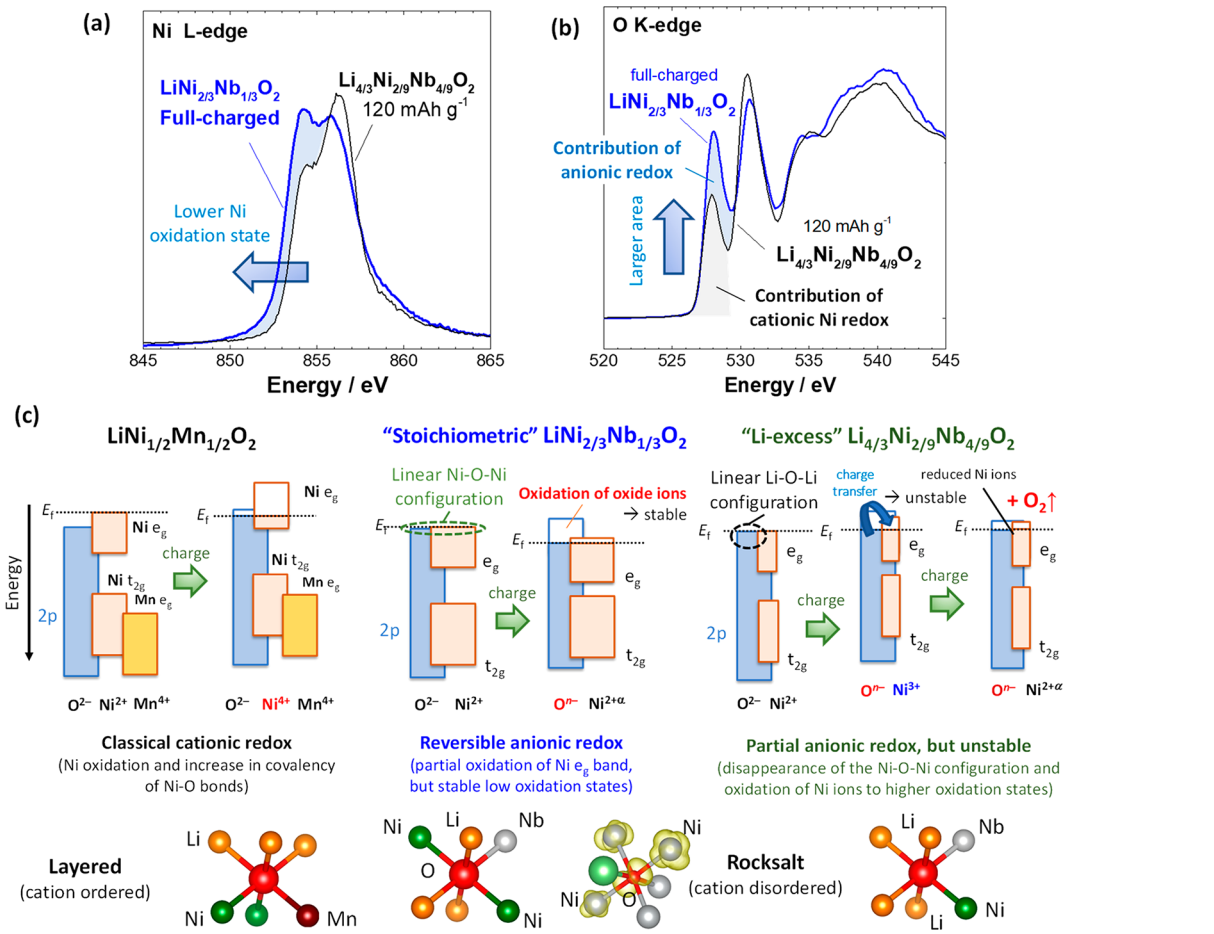

Figure 9. Summary of the activation and stabilization mechanism of anionic redox for Ni-based oxides. Comparison of (a) Ni L edge and (b) O K edge XAS spectra of stoichiometric $Li_{1-y}Ni_{2/3}Nb_{1/3}O_2$ (charged to 4.8 V) and Li-excess $Li_{4/3-y}Ni_{2/9}Nb_{4/9}O_2$ (half-charged to 120 mA h g^{-1}). The average oxidation state of the Ni ions is clearly lower for the stoichiometric sample in panel a, but a much higher peak intensity is noted at 528 eV in panel b. The appearance of this peak in the O K edge spectrum cannot be explained only by the oxidation of Ni ions, indicating that the formation of the unoccupied state for oxygen is largely responsible for this peak in the stoichiometric sample. (c) Schematic illustrations of cationic and anionic redox processes for a classical layered material $LiNi_{1/2}Mn_{1/2}O_2$, stoichiometric $LiNi_{2/3}Nb_{1/3}O_2$, and Li-excess $Li_{4/3}Ni_{2/9}Nb_{4/9}O_2$. The differences in the local environment of O, shown at the bottom, influence the activation and stabilization of anionic redox. For the linear Ni−O−Ni configuration of $LiNi_{2/3}Nb_{1/3}O_2$ with the disordered structure, the contribution of oxygen for charge compensation is large and thus Ni ions retain low oxidation states, which do not destabilize anionic redox. In contrast, the small coordination number of Ni to O for $Li_{4/3}Ni_{2/9}Nb_{4/9}O_2$ destabilizes anionic redox because of the formation of unstable Ni ions with higher oxidation states by delithiation. The linear Ni−O−Ni configuration is not formed in layered $LiNi_{1/2}Mn_{1/2}O_2$ and therefore anionic redox is not activated.

indicated at the same composition y in ordered $Li_{1-y}Ni_{2/3}Nb_{1/3}O_2$. This indicates the importance of the local coordination environment for each oxide ion, though averaged Bader charges for both Ni and O gradually change due to the strong hybridization between the Ni 3d and O 2p orbitals.

Such uniqueness of the linear Ni−O−Ni configuration for the disordered phase is further evidenced by the theoretical calculation of layered NiO_2, which was obtained via the oxidation of layered $LiNiO_2$ without Nb ions (Supporting Figure S23). After delithiation from layered $LiNiO_2$, zero-spin moments of O ions were found in NiO_2. This fact clearly indicates that the presence of Nb ions is not responsible for the large spin moments of the O ions. The zero-spin moments of oxygen were found for both layered NiO_2 and $Ni_{2/3}Nb_{1/3}O_2$ without the linear Ni−O−Ni environment. On the basis of these results, it was proposed that the formation of the linear Ni−O−Ni configuration is triggered by structural disordering, where the presence of Nb ions is essential to activate the anionic redox for Ni-based oxides. Note that approximately 10% anti-site defects form in $LiNi_{1/2}Mn_{1/2}O_2$,[27] leading to the formation of the liner Ni−O−Ni environment. However, the concentration is limited compared to that in disordered $LiNi_{2/3}Nb_{1/3}O_2$ and therefore cationic Ni redox is dominant in $Li_{1-y}Ni_{1/2}Mn_{1/2}O_2$, as shown in Supporting Figure S12.

Activation and Destabilization Mechanisms of Anionic Redox for Ni-Based Electrode Materials. In this manuscript, a systematic study of the binary system of Li_3NbO_4−NiO has been conducted. On the basis of experimental and theoretical findings, detailed stabilization and destabilization mechanisms of anionic redox for the stoichiometric and Li-excess systems are summarized in Figure 9. In classical layered materials, such as $LiNi_{1/2}Mn_{1/2}O_2$, the Fermi level of the sample consists of mainly Ni e_g orbitals. Through oxidation (electrochemical Li extraction), electrons are extracted from the Ni e_g orbitals near the Fermi level, corresponding to oxidation from Ni^{2+} to Ni^{4+}. The enhancement of covalency with O 2p orbitals after oxidation results in partial charge transfer from O ions to Ni ions (Figure 4b and

https://doi.org/10.1021/acscentsci.2c00238
ACS Cent. Sci. 2022, 8, 775−794

Supporting Figure S12). Nevertheless, on the basis of changes in the net spin moments of Ni and O obtained by theoretical calculations for the layered materials (Figure 8b and Supporting Figure S23), this system is essentially classified as the classical "cationic" redox process.

For $LiNi_{2/3}Nb_{1/3}O_2$, substitution with Nb^{5+}, which has a high ionic character, increases the energy of the O 2p orbitals relative to the Fermi level, leading to the increased accessibility of O redox upon charge and the lower contribution of Ni redox. In addition, Nb substitution triggers structural disordering; thus, the linear Ni−O−Ni configuration with a relatively strong antibonding character is formed near the Fermi level. Therefore, the large contribution of oxygen to charge compensation is achieved in this environment through σ-type interactions with the Ni e_g orbitals from both sides of the oxygen 2p orbitals (Figure 7c-1). Note that a similar phenomenon is also known for rocksalt NiO with a higher concentration of the Ni−O−Ni configuration. The band gap of NiO is sandwiched between the filled oxygen 2p band and the empty upper Hubbard band (Ni 3d band).[69] Additionally, NiO is known as a charge-transfer insulator.[70] Therefore, the oxidation of NiO (and the formation of $Ni_{1-x}O$) induces holes in the O 2p bands near the Fermi level without oxidation of Ni ions, as evidenced by theoretical and experimental XAS studies.[69] $Ni_{1-x}O$ is classified as a negative charge-transfer insulator with a narrow band gap, which is formed by the split of the O 2p band.[69] The partial oxidation of Ni ions also proceeds in $Li_{1-y}Ni_{2/3}Nb_{1/3}O_2$, as evidenced experimentally in Figure 4a and theoretically in Figure 8a. The partial oxidation of Ni ions possibly influences profile changes of the O K edge spectra. However, the average oxidation state of the Ni ions is lower when compared with thoseof layered materials (Figure 4b and Supporting Figure S13). When the XAS spectra of the fully charged stoichiometric and half-charged Li-excess samples are compared, the oxidation state of the Ni ions is higher for the half-charged Li-excess sample, as shown in Figure 9a. Nevertheless, a much larger peak area at 528 eV was observed in the O K edge XAS spectra of the fully charged stoichiometric sample, as shown in Figure 9b. From this comparison and the results of theoretical study, it was concluded that anionic redox with a σ-type interaction was observed at 528 eV in the O K edge spectra, which was found to have an energy similar to that of oxygen bonded to Ni^{3+} (Ni^{4+}) ions (see Figure 9b). For the case of the binary system of Li_3NbO_4−$LiMnO_2$, as well as other conventional Li_2MnO_3-based layered materials, the peak at 528 eV is not visible in the O K edge XAS spectra after charge.[55] Instead, a new peak appears at 530 eV, and the peak intensity evolves as the charge capacity increases. The origin of this peak has been explained by the formation of π-like bonds between Mn^{4+} (t_{2g}^3) and O 2p orbitals after lithium extraction[25,44] or the presence of filled π-orbitals for O_2 molecules.[17,34] After the oxidation of O in the Li−O−Li environment (essentially a nonbonding state), the anionic redox process is energetically stabilized by electron donation from Mn^{4+} ions, resulting in the rehybridization of the molecular orbitals and the formation of a weak π-type bond between Mn^{4+} and oxygen. On the basis of these differences in the O K edge XAS spectra profile evolution, the nature of the chemical bonds (σ- or π-type interaction with transition metals) is proposed to influence the profiles of the O K edge XAS spectra. Observations similar to those for the Li_3NbO_4−NiO system were also noted for the Fe^{3+} systems in which new peaks appear at *ca.* 528 eV, which was also observed for $SrFeO_3$ (Figure 4c).[54,55,71] Although Fe (d^5 high-spin configuration; t_{2g}^3 e_g^2) possibly stabilizes anionic redox through a σ-type interaction, oxygen loss is also a dominant process in this system, as observed in $Li_{4/3}Fe^{3+}{}_{1/3}Sb_{1/3}O_2$.[12]

Further enrichment of Li or Nb ions in the structure changes this scenario. Li or Nb enrichment inevitably reduces the Ni ion content, namely decreasing the coordination number of Ni to O. The concentration of oxygen in the linear Ni−O−Ni configuration is also reduced, and the linear Li−O−Li configuration is formed instead. As a result, Ni oxidation is unavoidable upon charge, similar to the Ni-based layered materials. Indeed, the average oxidation state of the Ni ions after charge is higher for the Li-excess phase than the disordered phase, as shown in Figure 9. Oxygen redox also occurs in the linear Li−O−Li configuration. Unstable Ni ions with higher oxidation states destabilize anionic redox and result in charge donation to Ni from O, causing Ni reduction and O_2 release, *i.e.*, reductive coupling.[12,55] Such Ni reduction upon "charge" is clearly visible in the XAS spectra shown in Figure 4a. The fraction of linear Ni−O−Ni configurations in the structure, which facilitate the stabilization of anionic redox through the formation of σ-type bonds, is too small and therefore oxygen loss cannot be suppressed for the Li-excess phase (Figure 3 and Supporting Figure S16 and S17).

Although the oxygen redox and its stabilization were evidenced for the stoichiometric phase, the reversible capacity is limited to only 85 mAh g^{-1}. This fact probably suggests that electrode kinetics in this system are essentially low. Additionally, the oxygen unoccupied state is not itinerant and is probably localized in this structure. Indeed, in contrast to the Ni−Nb system, highly reversible anionic redox and excellent electrode kinetics were achieved for $Li_{2-y}RuO_3$ with an itinerant electron system.[72] Nevertheless, as shown in Figure 2a, the reversible capacity for $Li_{12/11}Ni_{6/11}Nb_{4/11}O_2$ ($x = 0.40$) is further increased because of the increased percolation probability for Li migration in the structure due to Li enrichment.[73] Additionally, our recent work demonstrates that Li migration kinetics for the stoichiometric phase were drastically increased by the preparation of nanometer-sized samples.[74] Furthermore, anionic redox is more readily activated for nanometer-sized samples at lower operating temperatures.[75,76] Note that for $Li_{6/5}Ni_{2/5}Nb_{2/5}O_2$($x = 0.50$) the conversion reaction is clearly present after discharge, which suggests that anionic redox is destabilized in this composition. Because of the lower concentration of the linear Ni−O−Ni configuration in the structure, 40% Ni in the structure is not enough to suppress Ni oxidation and stabilize the unoccupied state of oxygen. Therefore, further increases in the energy density of positive electrode materials with anionic redox are anticipated through the optimization of particle sizes, the chemical composition, and the coordination environment for oxygen.

CONCLUSIONS

The reaction mechanisms of Li_3NbO_4−NiO binary oxides as positive electrode materials have been systematically examined, and the stabilization and destabilization mechanisms for anionic redox discussed. Direct evidence is presented for electrochemical anionic redox, which is stabilized through the formation of the linear Ni−O−Ni configuration and σ-type interactions with transition metal e_g orbitals. Soft XAS and theoretical studies reveal that reversible anionic redox with a small voltage hysteresis occurs in stoichiometric $LiNi_{2/3}Nb_{1/3}O_2$ with a cation-disordered Li/Ni arrangement. In addition, the importance of crystal structures is also noted. Anionic redox is

https://doi.org/10.1021/acscentsci.2c00238
ACS Cent. Sci. 2022, 8, 775−794

activated only in the disordered structure, and classical cationic redox is dominant in the ordered and layered structures. Although Li enrichment in the structure, and the formation of the Li−O−Li configuration, was proposed to be the necessary condition to activate anionic redox, careful analysis in this study with different structures/ and compositions reveals that structural disordering and the formation of the linear Ni−O−Ni configuration can also activate anionic redox. Moreover, the enrichment of the Li−O−Li configuration in this Ni-based system results in oxygen loss upon charge because of the loss of the Ni−O−Ni configuration and the formation of unstable Ni ions in the host structure. The activation and stabilization mechanisms of anionic redox found in stoichiometric $LiNi_{2/3}Nb_{1/3}O_2$ with a cation-disordered Li/Ni arrangement cannot be explained by the theory of anionic redox developed in Li-excess Mn-based oxides. Therefore, further research progress on anionic redox in electrode materials with different oxygen local structures is anticipated in the future. These findings provide a new direction for both the design of a class of 4 V positive electrode materials with reversible anionic redox through the engineering of the oxygen coordination environment and the development of high-energy lithium-ion batteries in the future.

EXPERIMENTAL METHODS

Synthesis of Materials. The target materials, generally with composition $xLi_3NbO_4-(1-x)NiO$, were synthesized by the solid-state method. Li_2CO_3 (98.5%, Kanto Kagaku), $NiCO_3 \cdot Ni(OH)_2 \cdot 4H_2O$ (Kishida Chemical), and Nb_2O_5 (99.9%; Wako Pure Chemical Industries) were mixed, followed by wet ball-milling with methanol at 300 rpm for 6 h. After drying, the obtained powder was pressed into pellets under a pressure of 20 MPa. The obtained pellets were calcined in air at 1000 °C for 48 or 2 h.

A polycrystalline sample of $SrFeO_3$ was synthesized via a solid-state reaction under high-pressure conditions. A mixture of stoichiometric amounts of $SrCO_3$ and Fe_2O_3 was first calcined at 1200 °C for 24 h in air. The obtained calcined powder was sealed in a Pt capsule with an oxidizing agent, $KClO_4$, and held at 4.0 GPa and 1000 °C for 30 m before being quenched to room temperature. The pressure was then reduced slowly to ambient. The reacted sample was washed with distilled water to remove the residual KCl and $KClO_4$.

Characterization. X-ray diffraction (XRD) patterns of the samples were collected using an X-ray diffractometer (D2 PHASER, Bruker) equipped with a one-dimensional X-ray detector using Cu Kα radiation generated at 300 W (30 kV and 10 mA) with a Ni filter. Structural analysis was carried out using RIETAN-FP.[77] Schematic illustrations of crystal structures were drawn using the program VESTA.[78] Neutron diffraction patterns were collected at BL09 (SPICA) in the Material and Life science Facility (MLF) of the Japan Proton Accelerator Research Complex (J-PARC).[79] Approximately 1 g of the powder samples was loaded in a cylindrical vanadium can with a 6 mm diameter (PV-6-F, Taiyo Koko Co. Ltd.). Structural analysis was carried out using Z-Rietveld.[80,81] The particle morphology of the samples was observed using a scanning electron microscope (JCM-6000, JEOL) with an acceleration voltage of 15 keV. Transmission electron microscopy (TEM) was conducted using a JEM-ARM200F (JEOL) microscope operated at 200 keV. The samples were dispersed in dimethyl carbonate and then supported on a copper grid.

For the electrochemical characterization, as-prepared oxides were mixed with acetylene black (AB, HS-100, Denka) and PVdF (no. 1100, Koreha), oxide/AB/PVdF = 80:10:10 wt %, and pasted on aluminum foil (Hosen Corp.) as a current collector. Metallic lithium (Honjo Metal) was used as a negative electrode. The electrolyte solution used was 1.0 mol dm^{-3} $LiPF_6$ dissolved in ethylene carbonate (EC)/dimethyl carbonate (DMC) 1:1 v/v (battery-grade, Kishida Chemical). A polyolefin microporous membrane (Celgard 2500) was used as a separator. Two-electrode-type Li cells (Tomcell Japan, type TJ-AC) were assembled in an Ar-filled glovebox. The cells were cycled at a rate of 5 or 10 mA g^{-1} at 50 °C. Sample loading ranged from 6−8 mg cm^{-2}, with sample thicknesses of 60−75 μm. The reversible capacity provided in this study was calculated on the basis of the masses of active materials.

Coin cells for *in operando* experiments were constructed from casings with 3 mm diameter holes and a stainless-steel spacer with a 5 mm hole, which allowed the X-rays to be transmitted through the cell. The cells were constructed in an Ar-filled glovebox, and the holes in the casing were sealed using Kapton tape on both the inside and the outside to prevent air exposure. In addition to the electrode in question ($LiNi_{2/3}Nb_{1/3}O_2$ (x = 0.33) and $Li_{4/3}Ni_{2/9}Nb_{4/9}O_2$ (x = 0.67), diameter of 12 mm), the coin cells contained a wave spring, a ∼1 mm thick Li metal plate, and a glass fiber separator with 110 μL of 1.0 M $LiPF_6$ in an EC/DMC (1:1 by volume) electrolyte solution (battery-grade, Sigma-Aldrich). The cells were transported in a vacuum sealed bag, and *in operando* experiments were carried out within 48 h of cell construction.

In operando synchrotron powder XRD experiments were performed at the Powder Diffraction beamline,[82] Australian Synchrotron, Clayton, Victoria, Australia. The coin cells were mounted on the beam using a custom-made holder and cycled using a Neware battery tester. During cycling, the cells were heated to 50 °C using a hot air blower, and the temperature was continuously monitored via a thermocouple mounted adjacent to the sample. A nominal X-ray beam energy of 18 keV (λ = 0.68745(2) Å) and beam dimensions 2.0 × 0.5 mm were used. The exact wavelength and the instrumental contribution to the peak broadening or profile were determined by calibration from an XRD pattern collected on a NIST LaB_6 660b line profile standard. The XRD data were collected using a Mythen position-sensitive silicon microstrip detector that moved between two positions (0.5° separation, 90 s exposure at each position), with a time resolution of 3.33 min per data set. The data sets were merged and normalized using the program PDViPeR, and Rietveld analysis was carried out with the Fullprof Suite software package.[83]

An online mass electrochemical mass spectrometry (OEMS) system was used as described in a previous work.[50] The custom-designed OEMS cell (Tomcell Japan) was comprised of electrode materials, lithium foil as the negative electrode, and 1 M $LiPF_6$ in a mixture of EC and DMC as the electrolyte solution. The assembled OEMS cell was rested in an Ar-filled glovebox for 2 h and linked to the OEMS apparatus in a constant-temperature container, maintaining a temperature of 25 °C. The OEMS cell was purged with Ar (99.9999%) for a total of 10 min to test the system. Cell pressure (16−18 psi) and the mass spectrum were also monitored at an open-circuit voltage at room temperature. The CO_2 gas evolution from DMC evaporation stabilized after 3 h and was then set as the background. The galvanostatic charging process was carried out

https://doi.org/10.1021/acscentsci.2c00238
ACS Cent. Sci. 2022, 8, 775−794

at a specific current of 10 mA g^{-1}. Gas analysis was conducted after the collection of gas products every 1 h.

Hard X-ray absorption spectroscopy (XAS) at the Ni K edge was performed at beamline BL-12C of the Photon Factory synchrotron source in Japan. Hard X-ray absorption spectra were collected with a silicon monochromator in the transmission mode. The intensities of the incident and transmitted X-rays were measured using an ionization chamber at room temperature. The composite electrodes were rinsed with dimethyl carbonate and sealed in a water-resistant polymer film (Kuraray, type EF-E) in an Ar-filled glovebox.

Soft X-ray absorption (XAS) spectra were collected at the BL-11 (O K edge and metal $L_{II,III}$ edges) beamline in the synchrotron facility of Ritsumeikan University (Synchrotron Radiation Center). The absorption spectra were collected in the fluorescence yield mode. Similar to the hard XAS measurement, the samples were prepared in an Ar-filled glovebox. The thus-prepared samples were placed on the spectrometer using a laboratory-made transfer vessel without air exposure.

First-principles calculations based on density functional theory (DFT)[84] were performed using the Vienna *ab initio* simulation package (VASP)[85,86] with both the modified Perdew−Burke−Ernzerhof generalized gradient approximation for a solid (PBEsol-GGA)[87,88] and the projector-augmented wave (PAW) method.[89] On-site Coulomb correction (GGA + *U*) was included for localized electronic states, and the *U* value for the Ni 3d states was set to 6.0 eV in accordance with the literature.[90] The Heyd−Scuseria−Ernzerhof (HSE06)[91,92] hybrid functional was also used to correct the self-interaction errors in accordance with the literature[41,93] and to obtain precise electronic structures. A kinetic cutoff energy was set to 750 eV, and *k*-point meshes were sampled such that the product of meshes and atoms was approximately 800. For example, 2 × 3 × 2 *k*-point meshes were employed for 18 formula units of $Li_{1-y}Ni_{2/3}Nb_{1/3}O_2$ (x = 0.33). These settings were found by convergence tests (<3 meV per $Li_{1-y}Ni_{2/3}Nb_{1/3}O_2$). Note that mesh densities were increased by a factor of approximately 1.5−2.0 when the density of states (DOS) profiles were computed for visualization purposes.

Safety Statement. No unexpected or unusually high safety hazards were encountered.

■ ASSOCIATED CONTENT

Supporting Information

The Supporting Information is available free of charge at https://pubs.acs.org/doi/10.1021/acscentsci.2c00238.

> Refined parameters and fitting results; structural parameters used for the theoretical calcultion; particle morphologies; TEM images; electron diffraction patterns; comparison of XRD patterns and SEM images for $LiNi_{2/3}Nb_{1/3}O_2$ synthesized by different conditions; capacity retention of $LiNi_{2/3}Nb_{1/3}O_2$ and $Li_{4/3}Ni_{2/9}Nb_{4/9}O_2$; initial charge−discharge profiles; *ex situ* XRD pattterns; *in operando* synchrotron XRD contour map; structural parameters; EXAFS spectra; Nb K edge, Ni L edge, and O K edge spectra; HR-TEM images; schematic illustration of hypothetical layered-type $LiNb_{1/3}Ni_{2/3}O_2$; and calculated net spin moments (PDF)

■ AUTHOR INFORMATION

Corresponding Author

Naoaki Yabuuchi − *Elements Strategy Initiative for Catalysts and Batteries, Kyoto University, Kyoto, Kyoto 615-8245, Japan; Department of Chemistry and Life Science and Advanced Chemical Energy Research Center, Yokohama National University, Yokohama, Kanagawa 240-8501, Japan;* orcid.org/0000-0002-9404-5693; Email: yabuuchi-naoaki-pw@ynu.ac.jp

Authors

Ryutaro Fukuma − *Department of Applied Chemistry, Tokyo Denki University, Tokyo, Tokyo 120-8551, Japan*

Maho Harada − *Frontier Research Institute for Materials Science (FRIMS), Nagoya Institute of Technology, Nagoya, Aichi 466-8555, Japan*

Wenwen Zhao − *Department of Applied Chemistry, Tokyo Denki University, Tokyo, Tokyo 120-8551, Japan*

Miho Sawamura − *Department of Applied Chemistry, Tokyo Denki University, Tokyo, Tokyo 120-8551, Japan*

Yusuke Noda − *GREEN and MaDiS/CMi², National Institute of Materials Science (NIMS), Tsukuba, Ibaraki 305-0047, Japan; Department of Information and Communication Engineering, Okayama Prefectural University, Soja, Okayama 719-1197, Japan;* orcid.org/0000-0003-0401-6731

Masanobu Nakayama − *Frontier Research Institute for Materials Science (FRIMS), Nagoya Institute of Technology, Nagoya, Aichi 466-8555, Japan; GREEN and MaDiS/CMi², National Institute of Materials Science (NIMS), Tsukuba, Ibaraki 305-0047, Japan; Elements Strategy Initiative for Catalysts and Batteries, Kyoto University, Kyoto, Kyoto 615-8245, Japan;* orcid.org/0000-0002-5113-053X

Masato Goto − *Institute for Chemical Research, Kyoto University, Uji, Kyoto 611-0011, Japan;* orcid.org/0000-0002-8198-7622

Daisuke Kan − *Institute for Chemical Research, Kyoto University, Uji, Kyoto 611-0011, Japan*

Yuichi Shimakawa − *Institute for Chemical Research, Kyoto University, Uji, Kyoto 611-0011, Japan;* orcid.org/0000-0003-1019-2512

Masao Yonemura − *High Energy Accelerator Research Organization, Institute of Materials Structure Science, Tsukuba, Ibaraki 305-0801, Japan; Department of Materials Structure Science, The Graduate University for Advanced Studies, SOKENDAI, Tokai, Ibaraki 319-1106, Japan*

Naohiro Ikeda − *Department of Chemistry and Life Science, Yokohama National University, Yokohama, Kanagawa 240-8501, Japan*

Ryuta Watanuki − *Elements Strategy Initiative for Catalysts and Batteries, Kyoto University, Kyoto, Kyoto 615-8245, Japan; Department of Chemistry and Life Science, Yokohama National University, Yokohama, Kanagawa 240-8501, Japan*

Henrik L. Andersen − *School of Chemistry, University of New South Wales, Sydney, NSW 2052, Australia*

Anita M. D'Angelo − *Australian Synchrotron, Clayton, VIC 3168, Australia*

Neeraj Sharma − *School of Chemistry, University of New South Wales, Sydney, NSW 2052, Australia;* orcid.org/0000-0003-1197-6343

Jiwon Park − *Department of Chemistry, KAIST Institute for NanoCentury, Korea Advanced Institute of Science and Technology (KAIST), Daejeon 34141, Republic of Korea;* orcid.org/0000-0002-2258-310X

Hye Ryung Byon − *Department of Chemistry, KAIST Institute for NanoCentury, Korea Advanced Institute of Science and Technology (KAIST), Daejeon 34141, Republic of Korea;* orcid.org/0000-0003-3692-6713
Sayuri Fukuyama − *Battery Materials Laboratory, BASF Japan Ltd., Amagasaki, Hyogo 660-0083, Japan*
Zhenji Han − *Battery Materials Laboratory, BASF Japan Ltd., Amagasaki, Hyogo 660-0083, Japan*
Hitoshi Fukumitsu − *Battery Materials Laboratory, BASF Japan Ltd., Amagasaki, Hyogo 660-0083, Japan*
Martin Schulz-Dobrick − *Battery Materials Laboratory, BASF Japan Ltd., Amagasaki, Hyogo 660-0083, Japan*
Keisuke Yamanaka − *SR Center, Ritsumeikan University, Kusatsu, Shiga 525-8577, Japan*
Hirona Yamagishi − *SR Center, Ritsumeikan University, Kusatsu, Shiga 525-8577, Japan*
Toshiaki Ohta − *SR Center, Ritsumeikan University, Kusatsu, Shiga 525-8577, Japan*

Complete contact information is available at: https://pubs.acs.org/10.1021/acscentsci.2c00238

Author Contributions

◓These authors contributed equally to this work.

Notes

The authors declare no competing financial interest.

■ ACKNOWLEDGMENTS

The neutron scattering experiment was approved by the Neutron Scattering Program Advisory Committee of IMSS, KEK (proposal no. 2014S10). The hard X-ray absorption work was performed under the approval of the Photon Factory Program Advisory Committee (proposal 2021G039). The soft XAS experiment was performed at the SR Center of Ritsumeikan University under the approval of the Program Review Committee (S16033 and S19006). N.Y. acknowledges partial support from Grant-in-Aid for Scientific Research, 19H05816 and 21H04698, from MEXT (Ministry of Education Culture, Sports, Science and Technology, Japan). M.N. is thankful for the partial support from Grant-in-Aid for Scientific Research (19H05815 and 20H02436) from MEXT. N.Y. and M.N. also acknowledge the partial support from the program "Elements Strategy Initiative to Form Core Research Center" (JPMXP0112101003) and from the Japan Science and Technology Agency (JST) through CREST Grant JPMJCR21O6. M.N. and Y.N. are thankful for the support from the "Materials research by Information Integration" Initiative (MI^2I) project of the "Support Program for Starting Up Innovation Hub" from the JST. H.L.A. acknowledges the support from the Carlsberg Foundation (Grants CF18-0519 and CF19-0143), and N.S. acknowledges support from the Australian Research Council (DP200100959 and FT200100707). We also gratefully acknowledge the Australian Nuclear Science and Technology Organisation (ANSTO) for the beamtime awarded at the powder diffraction instrument at the Australian Synchrotron. Jimmy Wu, Vittoria Pischedda, and Maxwell Ong are thanked for their assistance during the synchrotron PXRD beamtime.

■ REFERENCES

(1) Goodenough, J. B.; Kim, Y. Challenges for rechargeable Li batteries. *Chem. Mater.* **2010**, *22*, 587−603.
(2) Ohzuku, T.; Makimura, Y. Layered lithium insertion material of LiCo1/3Ni1/3Mn1/3O2 for lithium-ion batteries. *Chem. Lett.* **2001**, *30*, 642−643.
(3) Yabuuchi, N.; Ohzuku, T. Novel lithium insertion material of LiCo1/3Ni1/3Mn1/3O2 for advanced lithium-ion batteries. *J. Power Sources* **2003**, *119*, 171−174.
(4) Kim, U.-H.; Park, G.-T.; Conlin, P.; Ashburn, N.; Cho, K.; Yu, Y.-S.; Shapiro, D. A.; Maglia, F.; Kim, S.-J.; Lamp, P.; Yoon, C. S.; Sun, Y.-K. Cation ordered Ni-rich layered cathode for ultra-long battery life. *Energy Environ. Sci.* **2021**, *14*, 1573−1583.
(5) Kalyani, P.; Chitra, S.; Mohan, T.; Gopukumar, S. Lithium metal rechargeable cells using Li2MnO3 as the positive electrode. *J. Power Sources* **1999**, *80*, 103−106.
(6) Lu, Z. H.; MacNeil, D. D.; Dahn, J. R. Layered cathode materials Li[NixLi(1/3−2x/3)Mn(2/3-x/3)]O-2 for lithium-ion batteries. *Electrochem. Solid State Lett.* **2001**, *4*, A191−A194.
(7) Yu, D. Y. W.; Yanagida, K.; Kato, Y.; Nakamura, H. Electrochemical Activities in Li2MnO3. *J. Electrochem. Soc.* **2009**, *156*, A417−A424.
(8) Mohanty, D.; Kalnaus, S.; Meisner, R. A.; Rhodes, K. J.; Li, J.; Payzant, E. A.; Wood, D. L.; Daniel, C. Structural transformation of a lithium-rich Li1.2Co0.1Mn0.55Ni0.15O2 cathode during high voltage cycling resolved by in situ X-ray diffraction. *J. Power Sources* **2013**, *229*, 239−248.
(9) Yabuuchi, N.; Yamamoto, K.; Yoshii, K.; Nakai, I.; Nishizawa, T.; Omaru, A.; Toyooka, T.; Komaba, S. Structural and Electrochemical Characterizations on Li2MnO3-LiCoO2-LiCrO2 System as Positive Electrode Materials for Rechargeable Lithium Batteries. *J. Electrochem. Soc.* **2013**, *160*, A39−A45.
(10) Koga, H.; Croguennec, L.; Ménétrier, M.; Mannessiez, P.; Weill, F.; Delmas, C.; Belin, S. *J. Phys. Chem. C* **2014**, *118*, 5700−5709.
(11) Yabuuchi, N.; Yoshii, K.; Myung, S.-T.; Nakai, I.; Komaba, S. Detailed Studies of a High-Capacity Electrode Material for Rechargeable Batteries, Li2MnO3−LiCo1/3Ni1/3Mn1/3O2. *J. Am. Chem. Soc.* **2011**, *133*, 4404−4419.
(12) McCalla, E.; Sougrati, M. T.; Rousse, G.; Berg, E. J.; Abakumov, A.; Recham, N.; Ramesha, K.; Sathiya, M.; Dominko, R.; Van Tendeloo, G.; Novák, P.; Tarascon, J.-M. Understanding the Roles of Anionic Redox and Oxygen Release during Electrochemical Cycling of Lithium-Rich Layered Li4FeSbO6. *J. Am. Chem. Soc.* **2015**, *137*, 4804−4814.
(13) Sathiya, M.; Abakumov, A. M.; Foix, D.; Rousse, G.; Ramesha, K.; Saubanère, M.; Doublet, M. L.; Vezin, H.; Laisa, C. P.; Prakash, A. S.; Gonbeau, D.; VanTendeloo, G.; Tarascon, J. M. Origin of voltage decay in high-capacity layered oxide electrodes. *Nat. Mater.* **2015**, *14*, 230−238.
(14) Sathiya, M.; Rousse, G.; Ramesha, K.; Laisa, C. P.; Vezin, H.; Sougrati, M. T.; Doublet, M. L.; Foix, D.; Gonbeau, D.; Walker, W.; Prakash, A. S.; Ben Hassine, M.; Dupont, L.; Tarascon, J. M. Reversible anionic redox chemistry in high-capacity layered-oxide electrodes. *Nat. Mater.* **2013**, *12*, 827−835.
(15) Luo, K.; Roberts, M. R.; Guerrini, N.; Tapia-Ruiz, N.; Hao, R.; Massel, F.; Pickup, D. M.; Ramos, S.; Liu, Y. S.; Guo, J.; Chadwick, A. V.; Duda, L. C.; Bruce, P. G. Anion Redox Chemistry in the Cobalt Free 3d Transition Metal Oxide Intercalation Electrode Li-[Li0.2Ni0.2Mn0.6]O2. *J. Am. Chem. Soc.* **2016**, *138*, 11211−11218.
(16) Luo, K.; Roberts, M. R.; Hao, R.; Guerrini, N.; Pickup, D. M.; Liu, Y. S.; Edström, K.; Guo, J.; Chadwick, A. V.; Duda, L. C.; Bruce, P. G. Charge-compensation in 3d-transition-metal-oxide intercalation cathodes through the generation of localized electron holes on oxygen. *Nat. Chem.* **2016**, *8*, 684−691.
(17) House, R. A.; Maitra, U.; Pérez-Osorio, M. A.; Lozano, J. G.; Jin, L.; Somerville, J. W.; Duda, L. C.; Nag, A.; Walters, A.; Zhou, K.-J.; Roberts, M. R.; Bruce, P. G. Superstructure control of first-cycle voltage hysteresis in oxygen-redox cathodes. *Nature* **2020**, *577*, 502−508.
(18) Croy, J. R.; Kim, D.; Balasubramanian, M.; Gallagher, K.; Kang, S.-H.; Thackeray, M. M. Countering the Voltage Decay in High Capacity xLi2MnO3●(1−x)LiMO2 Electrodes (M = Mn, Ni, Co) for Li+-Ion Batteries. *J. Electrochem. Soc.* **2012**, *159*, A781−A790.

(19) Hu, E.; Yu, X.; Lin, R.; Bi, X.; Lu, J.; Bak, S.; Nam, K.-W.; Xin, H. L.; Jaye, C.; Fischer, D. A.; Amine, K.; Yang, X.-Q. Evolution of redox couples in Li- and Mn-rich cathode materials and mitigation of voltage fade by reducing oxygen release. *Nat. Energy* **2018**, *3*, 690−698.
(20) Yabuuchi, N.; Kubota, K.; Aoki, Y.; Komaba, S. Understanding Particle-Size-Dependent Electrochemical Properties of Li2MnO3-Based Positive Electrode Materials for Rechargeable Lithium Batteries. *J. Phys. Chem. C* **2016**, *120*, 875−885.
(21) Liu, W.; Oh, P.; Liu, X.; Myeong, S.; Cho, W.; Cho, J. Countering Voltage Decay and Capacity Fading of Lithium-Rich Cathode Material at 60 °C by Hybrid Surface Protection Layers. *Adv. Energy Mater.* **2015**, *5*, 1500274.
(22) Zhang, S.; Gu, H.; Pan, H.; Yang, S.; Du, W.; Li, X.; Gao, M.; Liu, Y.; Zhu, M.; Ouyang, L.; Jian, D.; Pan, F. A Novel Strategy to Suppress Capacity and Voltage Fading of Li- and Mn-Rich Layered Oxide Cathode Material for Lithium-Ion Batteries. *Adv. Energy Mater.* **2017**, *7*, 1601066.
(23) Croy, J. R.; Gallagher, K. G.; Balasubramanian, M.; Chen, Z.; Ren, Y.; Kim, D.; Kang, S.-H.; Dees, D. W.; Thackeray, M. M. Examining Hysteresis in Composite xLi2MnO3·(1−x)LiMO2 Cathode Structures. *J. Phys. Chem. C* **2013**, *117*, 6525−6536.
(24) Tsuchimoto, A.; Shi, X.-M.; Kawai, K.; Mortemard de Boisse, B.; Kikkawa, J.; Asakura, D.; Okubo, M.; Yamada, A. Nonpolarizing oxygen-redox capacity without O-O dimerization in Na2Mn3O7. *Nat. Commun.* **2021**, *12*, 631.
(25) Kitchaev, D. A.; Vinckeviciute, J.; Van der Ven, A. Delocalized Metal−Oxygen π-Redox Is the Origin of Anomalous Nonhysteretic Capacity in Li-Ion and Na-Ion Cathode Materials. *J. Am. Chem. Soc.* **2021**, *143*, 1908−1916.
(26) Yabuuchi, N.; Tahara, Y.; Komaba, S.; Kitada, S.; Kajiya, Y. Synthesis and Electrochemical Properties of Li4MoO5−NiO Binary System as Positive Electrode Materials for Rechargeable Lithium Batteries. *Chem. Mater.* **2016**, *28*, 416−419.
(27) Zhao, W.; Yamaguchi, K.; Sato, T.; Yabuuchi, N. Li4/3Ni1/3Mo1/3O2 − LiNi1/2Mn1/2O2 Binary System as High Capacity Positive Electrode Materials for Rechargeable Lithium Batteries. *J. Electrochem. Soc.* **2018**, *165*, A1357−A1362.
(28) Hafiz, H.; Suzuki, K.; Barbiellini, B.; Tsuji, N.; Yabuuchi, N.; Yamamoto, K.; Orikasa, Y.; Uchimoto, Y.; Sakurai, Y.; Sakurai, H.; Bansil, A.; Viswanathan, V. Tomographic reconstruction of oxygen orbitals in lithium-rich battery materials. *Nature* **2021**, *594*, 213−216.
(29) Lee, J.; Papp, J. K.; Clément, R. J.; Sallis, S.; Kwon, D.-H.; Shi, T.; Yang, W.; McCloskey, B. D.; Ceder, G. Mitigating oxygen loss to improve the cycling performance of high capacity cation-disordered cathode materials. *Nat. Commun.* **2017**, *8*, 981.
(30) House, R. A.; Jin, L.; Maitra, U.; Tsuruta, K.; Somerville, J. W.; Förstermann, D. P.; Massel, F.; Duda, L.; Roberts, M. R.; Bruce, P. G. Lithium manganese oxyfluoride as a new cathode material exhibiting oxygen redox. *Energy Environ. Sci.* **2018**, *11*, 926−932.
(31) Lee, J.; Kitchaev, D. A.; Kwon, D.-H.; Lee, C.-W.; Papp, J. K.; Liu, Y.-S.; Lun, Z.; Clément, R. J.; Shi, T.; McCloskey, B. D.; Guo, J.; Balasubramanian, M.; Ceder, G. Reversible Mn2+/Mn4+ double redox in lithium-excess cathode materials. *Nature* **2018**, *556*, 185−190.
(32) Jacquet, Q.; Iadecola, A.; Saubanère, M.; Li, H.; Berg, E. J.; Rousse, G.; Cabana, J.; Doublet, M.-L.; Tarascon, J.-M. Charge Transfer Band Gap as an Indicator of Hysteresis in Li-Disordered Rock Salt Cathodes for Li-Ion Batteries. *J. Am. Chem. Soc.* **2019**, *141*, 11452−11464.
(33) Campéon, B. D. L.; Yabuuchi, N. Fundamentals of metal oxide/oxyfluoride electrodes for Li-/Na-ion batteries. *Chem. Phys. Rev.* **2021**, *2*, 041306.
(34) Sharpe, R.; House, R. A.; Clarke, M. J.; Förstermann, D.; Marie, J.-J.; Cibin, G.; Zhou, K.-J.; Playford, H. Y.; Bruce, P. G.; Islam, M. S. Redox Chemistry and the Role of Trapped Molecular O2 in Li-Rich Disordered Rocksalt Oxyfluoride Cathodes. *J. Am. Chem. Soc.* **2020**, *142*, 21799−21809.
(35) Lun, Z.; Ouyang, B.; Kitchaev, D. A.; Clément, R. J.; Papp, J. K.; Balasubramanian, M.; Tian, Y.; Lei, T.; Shi, T.; McCloskey, B. D.; Lee, J.; Ceder, G. Improved Cycling Performance of Li-Excess Cation-Disordered Cathode Materials upon Fluorine Substitution. *Adv. Energy Mater.* **2019**, *9*, 1802959.
(36) Okuoka, S.; Ogasawara, Y.; Suga, Y.; Hibino, M.; Kudo, T.; Ono, H.; Yonehara, K.; Sumida, Y.; Yamada, Y.; Yamada, A.; Oshima, M.; Tochigi, E.; Shibata, N.; Ikuhara, Y.; Mizuno, N. A New Sealed Lithium-Peroxide Battery with a Co-Doped Li_2O Cathode in a Super-concentrated Lithium Bis(fluorosulfonyl)amide Electrolyte. *Sci. Rep.* **2015**, *4*, 5684.
(37) Kobayashi, H.; Hibino, M.; Ogasawara, Y.; Yamaguchi, K.; Kudo, T.; Okuoka, S.-i.; Yonehara, K.; Ono, H.; Sumida, Y.; Oshima, M.; Mizuno, N. Improved performance of Co-doped Li2O cathodes for lithium-peroxide batteries using LiCoO2 as a dopant source. *J. Power Sources* **2016**, *306*, 567−572.
(38) Zhan, C.; Yao, Z.; Lu, J.; Ma, L.; Maroni, V. A.; Li, L.; Lee, E.; Alp, E. E.; Wu, T.; Wen, J.; Ren, Y.; Johnson, C.; Thackeray, M. M.; Chan, M. K. Y.; Wolverton, C.; Amine, K. Enabling the high capacity of lithium-rich anti-fluorite lithium iron oxide by simultaneous anionic and cationic redox. *Nature Energy* **2017**, *2*, 963−971.
(39) Zhu, Z.; Kushima, A.; Yin, Z.; Qi, L.; Amine, K.; Lu, J.; Li, J. Anion-redox nanolithia cathodes for Li-ion batteries. *Nat. Energy* **2016**, *1*, 16111.
(40) Zheng, J.; Teng, G.; Yang, J.; Xu, M.; Yao, Q.; Zhuo, Z.; Yang, W.; Liu, Q.; Pan, F. Mechanism of Exact Transition between Cationic and Anionic Redox Activities in Cathode Material Li2FeSiO4. *J. Phys. Chem. Lett.* **2018**, *9*, 6262−6268.
(41) Seo, D.-H.; Lee, J.; Urban, A.; Malik, R.; Kang, S.; Ceder, G. The structural and chemical origin of the oxygen redox activity in layered and cation-disordered Li-excess cathode materials. *Nat. Chemi* **2016**, *8*, 692−697.
(42) Maitra, U.; House, R. A.; Somerville, J. W.; Tapia-Ruiz, N.; Lozano, J. G.; Guerrini, N.; Hao, R.; Luo, K.; Jin, L.; Pérez-Osorio, M. A.; Massel, F.; Pickup, D. M.; Ramos, S.; Lu, X.; McNally, D. E.; Chadwick, A. V.; Giustino, F.; Schmitt, T.; Duda, L. C.; Roberts, M. R.; Bruce, P. G. Oxygen redox chemistry without excess alkali-metal ions in Na2/3[Mg0.28Mn0.72]O2. *Nat. Chem.* **2018**, *10*, 288.
(43) Yabuuchi, N. Solid-state Redox Reaction of Oxide Ions for Rechargeable Batteries. *Chem. Lett.* **2017**, *46*, 412−422.
(44) Okubo, M.; Yamada, A. Molecular Orbital Principles of Oxygen-Redox Battery Electrodes. *ACS Appl. Mater. Interfaces* **2017**, *9*, 36463−36472.
(45) Sudayama, T.; Uehara, K.; Mukai, T.; Asakura, D.; Shi, X.-M.; Tsuchimoto, A.; Mortemard de Boisse, B.; Shimada, T.; Watanabe, E.; Harada, Y.; Nakayama, M.; Okubo, M.; Yamada, A. Multiorbital bond formation for stable oxygen-redox reaction in battery electrodes. *Energy Environ. Sci.* **2020**, *13*, 1492−1500.
(46) Yabuuchi, N.; Takeuchi, M.; Nakayama, M.; Shiiba, H.; Ogawa, M.; Nakayama, K.; Ohta, T.; Endo, D.; Ozaki, T.; Inamasu, T.; Sato, K.; Komaba, S. High-capacity electrode materials for rechargeable lithium batteries: Li_3NbO_4-based system with cation-disordered rocksalt structure. *Proc. Natl. Acad. Sci.* **2015**, *112*, 7650−7655.
(47) Assat, G.; Tarascon, J.-M. Fundamental understanding and practical challenges of anionic redox activity in Li-ion batteries. *Nat. Energy* **2018**, *3*, 373−386.
(48) Shannon, R. D. Revised Effective Ionic-Radii and Systematic Studies of Interatomic Distances in Halides and Chalcogenides. *Acta Crystallogr., Sect. A* **1976**, *32*, 751−767.
(49) Mather, G. C.; West, A. R. Continuous Order−Disorder Transition in Li3Ni2NbO6and Cr-Doped Li3Ni2NbO6Rock Salt Structures. *J. Solid State Chem.* **1996**, *124*, 214−219.
(50) Bonnet-Mercier, N.; Wong, R. A.; Thomas, M. L.; Dutta, A.; Yamanaka, K.; Yogi, C.; Ohta, T.; Byon, H. R. A structured three-dimensional polymer electrolyte with enlarged active reaction zone for Li−O2 batteries. *Sci. Rep.* **2015**, *4*, 7127.
(51) Metzger, M.; Strehle, B.; Solchenbach, S.; Gasteiger, H. A. Origin of H-2 Evolution in LIBs: H2O Reduction vs. Electrolyte Oxidation. *J. Electrochem. Soc.* **2016**, *163*, A798−A809.
(52) Rougier, A.; Delmas, C.; Chadwick, A. V. Non-cooperative Jahn-Teller effect in LiNiO2: An EXAFS study. *Solid State Commun.* **1995**, *94*, 123−127.

https://doi.org/10.1021/acscentsci.2c00238
ACS Cent. Sci. 2022, 8, 775−794

(53) Ito, A.; Sato, Y.; Sanada, T.; Hatano, M.; Horie, H.; Ohsawa, Y. In situ X-ray absorption spectroscopic study of Li-rich layered cathode material Li[Ni0.17Li0.2Co0.07Mn0.56]O2. *J. Power Sources* **2011**, *196*, 6828−6834.
(54) Matsuhara, T.; Tsuchiya, Y.; Yamanaka, K.; Mitsuhara, K.; Ohta, T.; Yabuuchi, N. Synthesis and Electrode Performance of Li4MoO5-LiFeO2 Binary System as Positive Electrode Materials for Rechargeable Lithium Batteries. *Electrochemistry* **2016**, *84*, 797−801.
(55) Yabuuchi, N.; Nakayama, M.; Takeuchi, M.; Komaba, S.; Hashimoto, Y.; Mukai, T.; Shiiba, H.; Sato, K.; Kobayashi, Y.; Nakao, A.; Yonemura, M.; Yamanaka, K.; Mitsuhara, K.; Ohta, T. Origin of Stabilization and Destabilization in Solid-State Redox Reaction of Oxide Ions for Lithium-Ion Batteries. *Nat. Commun.* **2016**, *7*, 13814.
(56) Hu, N.; Tang, Z.; Shen, P. K. Hierarchical NiO nanobelt film array as an anode for lithium-ion batteries with enhanced electrochemical performance. *RSC Adv.* **2018**, *8*, 26589−26595.
(57) Gu, M.; Belharouak, I.; Zheng, J.; Wu, H.; Xiao, J.; Genc, A.; Amine, K.; Thevuthasan, S.; Baer, D. R.; Zhang, J.-G.; Browning, N. D.; Liu, J.; Wang, C. Formation of the Spinel Phase in the Layered Composite Cathode Used in Li-Ion Batteries. *ACS Nano* **2013**, *7*, 760−767.
(58) Yoon, W.-S.; Chung, K. Y.; McBreen, J.; Fischer, D. A.; Yang, X.-Q. Changes in electronic structure of the electrochemically Li-ion deintercalated LiNiO2 system investigated by soft X-ray absorption spectroscopy. *J. Power Sources* **2006**, *163*, 234−237.
(59) Yoon, W.-S.; Balasubramanian, M.; Chung, K. Y.; Yang, X.-Q.; McBreen, J.; Grey, C. P.; Fischer, D. A. Investigation of the Charge Compensation Mechanism on the Electrochemically Li-Ion Deintercalated Li1-xCo1/3Ni1/3Mn1/3O2 Electrode System by Combination of Soft and Hard X-ray Absorption Spectroscopy. *J. Am. Chem. Soc.* **2005**, *127*, 17479−17487.
(60) Abbate, M.; De Groot, F. M. F.; Fuggle, J. C.; Fujimori, A.; Strebel, O.; Lopez, M. F.; Domke, M.; Kaindl, G.; Sawatzky, G. A.; Takano, M.; Takeda, Y.; Eisaki, H.; Uchida, S. Controlled-valence properties of La1-xSrxFeO3 and La1-xSrxMnO3 studied by soft-x-ray absorption spectroscopy. *Phys. Rev. B* **1992**, *46*, 4511−4519.
(61) Zhang, K. H. L.; Du, Y.; Sushko, P. V.; Bowden, M. E.; Shutthanandan, V.; Sallis, S.; Piper, L. F. J.; Chambers, S. A. Hole-induced insulator-to-metal transition in La1-xSrxCrO3 epitaxial films. *Phys. Rev. B* **2015**, *91*, 155129.
(62) Reed, J.; Ceder, G. Role of Electronic Structure in the Susceptibility of Metastable Transition-Metal Oxide Structures to Transformation. *Chem. Rev.* **2004**, *104*, 4513−4534.
(63) Nakayama, M.; Nishii, K.; Watanabe, K.; Tanibata, N.; Takeda, H.; Itoh, T.; Asaka, T. First-principles study of the morphology and surface structure of LaCoO3 and La0.5Sr0.5Fe0.5Co0.5O3 perovskites as air electrodes for solid oxide fuel cells. *Science and Technology of Advanced Materials: Methods* **2021**, *1*, 24−33.
(64) Jain, A.; Hautier, G.; Ong, S. P.; Moore, C. J.; Fischer, C. C.; Persson, K. A.; Ceder, G. Formation enthalpies by mixing GGA and GGA + U calculations. *Phys. Rev. B* **2011**, *84*, 045115.
(65) Hautier, G.; Ong, S. P.; Jain, A.; Moore, C. J.; Ceder, G. Accuracy of density functional theory in predicting formation energies of ternary oxides from binary oxides and its implication on phase stability. *Phys. Rev. B* **2012**, *85*, 155208.
(66) Zhou, F.; Marianetti, C. A.; Cococcioni, M.; Morgan, D.; Ceder, G. Phase separation in ${\mathrm{Li}}_{x}{\mathrm{FePO}}_{4}$ induced by correlation effects. *Phys. Rev. B* **2004**, *69*, 201101.
(67) Chevrier, V. L.; Ong, S. P.; Armiento, R.; Chan, M. K. Y.; Ceder, G. Hybrid density functional calculations of redox potentials and formation energies of transition metal compounds. *Phys. Rev. B* **2010**, *82*, 075122.
(68) Sato, K.; Nakayama, M.; Glushenkov, A. M.; Mukai, T.; Hashimoto, Y.; Yamanaka, K.; Yoshimura, M.; Ohta, T.; Yabuuchi, N. Na-Excess Cation-Disordered Rocksalt Oxide: Na1.3Nb0.3Mn0.4O2. *Chem. Mater.* **2017**, *29*, 5043−5047.
(69) Peng, H. Y.; Li, Y. F.; Lin, W. N.; Wang, Y. Z.; Gao, X. Y.; Wu, T. Deterministic conversion between memory and threshold resistive switching via tuning the strong electron correlation. *Sci. Rep.* **2012**, *2*, 442.
(70) Kuneš, J.; Anisimov, V. I.; Skornyakov, S. L.; Lukoyanov, A. V.; Vollhardt, D. NiO: Correlated Band Structure of a Charge-Transfer Insulator. *Phys. Rev. Lett.* **2007**, *99*, 156404.
(71) Glazier, S. L.; Li, J.; Zhou, J.; Bond, T.; Dahn, J. R. Characterization of Disordered Li(1+x)Ti2xFe(1−3x)O2 as Positive Electrode Materials in Li-Ion Batteries Using Percolation Theory. *Chem. Mater.* **2015**, *27*, 7751−7756.
(72) Yabuuchi, N. Material Design Concept of Lithium-Excess Electrode Materials with Rocksalt-Related Structures for Rechargeable Non-Aqueous Batteries. *Chem. Rec* **2019**, *19*, 690−707.
(73) Lee, J.; Urban, A.; Li, X.; Su, D.; Hautier, G.; Ceder, G. Unlocking the Potential of Cation-Disordered Oxides for Rechargeable Lithium Batteries. *Science* **2014**, *343*, 519−522.
(74) Sato, T.; Sato, K.; Zhao, W.; Kajiya, Y.; Yabuuchi, N. Metastable and nanosize cation-disordered rocksalt-type oxides: revisit of stoichiometric LiMnO2 and NaMnO2. *J. Mater. Chem. A* **2018**, *6*, 13943−13951.
(75) Kobayashi, Y.; Sawamura, M.; Kondo, S.; Harada, M.; Noda, Y.; Nakayama, M.; Kobayakawa, S.; Zhao, W.; Nakao, A.; Yasui, A.; Rajendra, H. B.; Yamanaka, K.; Ohta, T.; Yabuuchi, N. Activation and stabilization mechanisms of anionic redox for Li storage applications: Joint experimental and theoretical study on Li2TiO3−LiMnO2 binary system. *Mater. Today* **2020**, *37*, 43−55.
(76) Sawamura, M.; Kobayakawa, S.; Kikkawa, J.; Sharma, N.; Goonetilleke, D.; Rawal, A.; Shimada, N.; Yamamoto, K.; Yamamoto, R.; Zhou, Y.; Uchimoto, Y.; Nakanishi, K.; Mitsuhara, K.; Ohara, K.; Park, J.; Byon, H. R.; Koga, H.; Okoshi, M.; Ohta, T.; Yabuuchi, N. Nanostructured LiMnO2 with Li3PO4 Integrated at the Atomic Scale for High-Energy Electrode Materials with Reversible Anionic Redox. *ACS Cent. Sci.* **2020**, *6*, 2326−2338.
(77) Izumi, F.; Momma, K. Three-Dimensional Visualization in Powder Diffraction. *Solid State Phenomena* **2007**, *130*, 15−20.
(78) Momma, K.; Izumi, F. VESTA 3 for three-dimensional visualization of crystal, volumetric and morphology data. *J. Appl. Crystallogr.* **2011**, *44*, 1272−1276.
(79) Yonemura, M.; Mori, K.; Kamiyama, T.; Fukunaga, T.; Torii, S.; Nagao, M.; Ishikawa, Y.; Onodera, Y.; Adipranoto, D. S.; Arai, H.; Uchimoto, Y.; Ogumi, Z. Development of SPICA, New Dedicated Neutron Powder Diffractometer for Battery Studies. *J. Phys. Conf. Ser.* **2014**, *502*, 012053.
(80) Oishi, R.; Yonemura, M.; Nishimaki, Y.; Torii, S.; Hoshikawa, A.; Ishigaki, T.; Morishima, T.; Mori, K.; Kamiyama, T. Rietveld analysis software for J-PARC. *Nucl.l Instrum. Methods Phys. Res. A* **2009**, *600*, 94−96.
(81) Oishi-Tomiyasu, R.; Yonemura, M.; Morishima, T.; Hoshikawa, A.; Torii, S.; Ishigaki, T.; Kamiyama, T. Application of Matrix Decomposition Algorithms for Singular Matrices to The Pawley Method in Z-Rietveld. *J. Appl. Crystallogr.* **2012**, *45*, 299−308.
(82) Wallwork, K. S.; Kennedy, B. J.; Wang, D. The high resolution powder diffraction beamline for the Australian Synchrotron. *Synchrotron Radiation Instrumentation, Pts 1 and 2* **2006**, *879*, 879−882.
(83) Rodriguez-Carvajal, J. Recent Advances in Magnetic-Structure Determination by Neutron Powder Diffraction. *Physica B Condens. Matter* **1993**, *192*, 55−69.
(84) Hohenberg, P.; Kohn, W. The Inhomogeneous Electron Gas. *Phys. Rev.* **1964**, *136*, B864.
(85) Kresse, G.; Furthmüller, J. Efficient iterative schemes for ab initio total-energy calculations using a plane-wave basis set. *Physical Review B - Condensed Matter and Materials Physics* **1996**, *54*, 11169−11186.
(86) Kresse, G.; Furthmüller, J. Efficiency of ab-initio total energy calculations for metals and semiconductors using a plane-wave basis set. *Comput. Mater. Sci.* **1996**, *6*, 15−50.
(87) Perdew, J.; Burke, K.; Ernzerhof, M. Generalized Gradient Approximation Made Simple. *Physical review letters* **1996**, *77*, 3865−3868.

(88) Mattsson, A. E.; Armiento, R.; Mattsson, T. R. Comment on "Restoring the Density-Gradient Expansion for Exchange in Solids and Surfaces". *Phys. Rev. Lett.* **2008**, *101*, 239701.
(89) Blöchl, P. E. Projector augmented-wave method. *Phys. Rev. B* **1994**, *50*, 17953−17979.
(90) Hautier, G.; Ong, S. P.; Jain, A.; Moore, C. J.; Ceder, G. Accuracy of density functional theory in predicting formation energies of ternary oxides from binary oxides and its implication on phase stability. *Physical Review B - Condensed Matter and Materials Physics* **2012**, *85*, 155208.
(91) Heyd, J.; Scuseria, G. E.; Ernzerhof, M. Hybrid functionals based on a screened Coulomb potential. *J. Chem. Phys.* **2003**, *118*, 8207−8215.
(92) Da Silva, J. L. F.; Ganduglia-Pirovano, M. V.; Sauer, J.; Bayer, V.; Kresse, G. Hybrid functionals applied to rare-earth oxides: The example of ceria. *Phys. Rev. B* **2007**, *75*, 045121.
(93) Da Silva, J. L. F.; Ganduglia-Pirovano, M. V.; Sauer, J.; Bayer, V.; Kresse, G. Hybrid functionals applied to rare-earth oxides: The example of ceria. *Physical Review B - Condensed Matter and Materials Physics* **2007**, *75*, 045121.

https://doi.org/10.1021/acscentsci.2c00238
ACS Cent. Sci. 2022, 8, 775−794